Version of Record: https://www.sciencedirect.com/science/article/pii/S001021802100674X
Manuscript_06721105af026e0b73d7cb16d6ad8fbf

Nonlinear dynamics of combustor azimuthal modes: Experiments and modeling

Jeongwon Kim[a,*], Tony John[a], Subodh Adhikari[a], David Wu[a], Benjamin Emerson[a], Vishal Acharya[a], Mitsunori Isono[b], Toshihiko Saito[b], Timothy Lieuwen[a]

[a] Ben T. Zinn Combustion Laboratory, Georgia Institute of Technology, Atlanta, GA, 30318, USA
[b] Mitsubishi Heavy Industries, Ltd, Takasago-shi, Hyogo, 676-8686, Japan

This paper provides an experimental and theoretical investigation of azimuthal instabilities in a lean, premixed combustor. It presents data from a high Reynolds number, industrial-scale facility with multiple fuel stages that enable variation of radial and azimuthal symmetries. The combustor exhibits a variety of behaviors – including standing, spinning, mixed waves, and intermittent behaviors, as well as periodic limit cycles and quasi-periodic oscillations – depending upon varying power and azimuthal symmetry. A second key objective of this paper is to present a weakly nonlinear framework that is used to understand and interpret these results, showing the influence of eigenmode degeneracy, background noise, and azimuthal non-uniformities in mean quantities such as temperature and flame-acoustic coupling. In particular, this analysis shows the importance of the linear instability growth/damping rate and azimuthal non-uniformities in controlling the relative prominence of standing, spinning, or mixed waves at the limit cycle, as well as the preference in the spinning direction. It also shows the conditions under which single frequency or quasi-periodic oscillations are dominant, and how these are more fundamentally influenced by azimuthal non-uniformities and background noise.

Keywords: Thermoacoustic, Low order model, Nonlinear dynamics, Method of averaging, Phase portrait

Nomenclature

A	Magnitude of horizontal standing mode	t	Time
B	Magnitude of vertical standing mode	U	Potential
B_{ij}	Tayler series coefficients in source term	α	Linear damping rate
b_{ij}	Azimuthal average value of B_{ij}	β	Linear growth rate
CW	Clockwise	Γ	White noise intensity
CCW	Counter-clockwise	γ	Ratio between linear damping/ growth rate
C_{ij}	Fourier coefficients for cosine terms		
c	Speed of sound	Δ	Normalized frequency spacing
F	Magnitude of CCW spinning mode	ΔSR	Amplitude of spin ratio modulation
FP	Fixed point	$\Delta\omega$	Difference between two frequencies
f	Amplitude of CCW spinning mode	ζ	Spatially averaged noise term

* Corresponding author.
E-mail address: jwkim89@gatech.edu

© 2021 published by Elsevier. This manuscript is made available under the Elsevier user license
https://www.elsevier.com/open-access/userlicense/1.0/

f_{mod}	Spin ratio modulation frequency
G	Magnitude of CW spinning mode
g	Amplitude of CW spinning mode
h	General source term in wave equation
i	Imaginary unit
$\dot{m}$	Mass flow rate
n	Azimuthal wavenumber
OR	Outer ratio
PR	Pilot ratio
p	Acoustic pressure
$\bar{p}$	Static pressure
R	Chamber radius
S_{ij}	Fourier coefficients for sine terms
SR	Spin ratio
η_1, η_2	Amplitudes of two standing eigenmodes
θ	Azimuthal coordinate
θ_a	Azimuthal location of pressure anti-node
ξ_1, ξ_2	Additive/parametric noise term
τ	Slow time scale
φ	Phase difference between two standing eigenmodes
φ_{FG}	Phase difference between two spinning eigenmodes
ω_1, ω_2	Natural frequencies of two standing eigenmodes
$\bar{\omega}$	Averaged frequency

1. Introduction

Combustion instabilities are a key challenge in lean, premixed combustion systems. They occur when unsteady heat release adds energy to the acoustic field, leading to excitation of the combustor's acoustic modes [1]. Instabilities lead to hardware damage and restrict the conditions at which these systems can operate [2].

These instabilities can occur over a wide range of frequencies associated with different types of acoustic modes. For example, annular combustors exhibit axial [3, 4], azimuthal [5-7], or radial oscillations, whose frequencies scale with the speed of sound divided by combustor length, circumference, and annular gap width, respectively. For this reason, azimuthal oscillations often occur at the lowest frequencies and radial oscillations at the highest frequencies. Similarly, can-type combustors exhibit axial, azimuthal, or radial modes, with observed frequencies varying by an order of magnitude [8-12].

Due to rotational symmetries, azimuthal modes have additional degrees of freedom relative to radial and axial modes in how they manifest themselves and nonlinearly interact. First, they can exist as standing waves with well-defined spatial nodes and anti-nodes, whose location stays fixed or drifts slowly relative to the speed of sound. In contrast, nodal lines are fixed for axial and radial modes. Second, they can exist as spinning waves that propagate in clockwise (CW) or counter-clockwise (CCW) direction. Lastly, they can exist as mixed waves, which are a linear combination of spinning and standing waves. Furthermore, the combustor can exhibit a relatively fixed modal character, or intermittently switch between one wave direction and another, or between standing and spinning wave dominant. Experimental studies have reported standing, spinning, and mixed waves depending on the operating conditions such as equivalence ratio [13, 14], wall temperature [15], swirl intensity [16], fuel staging [17], and nozzle geometry [18, 19]. Numerical studies have reported similar behaviors of different azimuthal modes [20-24].

Based on these observations, numerous studies have proposed models to capture the physics controlling which type of mode is present and its amplitude. These are nonlinear models, as linear models can allow for any arbitrary superposition of disturbances. For example, Eq. (1) represents general two coupled 2nd order harmonic oscillators.

$$\ddot{\eta}_1 + \alpha_1\dot{\eta}_1 + \omega_1^2\eta_1 = f_{NL,1}(\eta_1, \eta_2, \dot{\eta}_1, \dot{\eta}_2)$$
$$\ddot{\eta}_2 + \alpha_2\dot{\eta}_2 + \omega_2^2\eta_2 = f_{NL,2}(\eta_1, \eta_2, \dot{\eta}_1, \dot{\eta}_2) \quad (1)$$

Here, $\eta_1(t)$ and $\eta_2(t)$ describe the time-varying amplitudes of two eigenmodes that are coupled through the nonlinear terms on the right hand side. Both eigenmodes are linearly stable when the linear damping terms, $\alpha_{1,2}$, are positive, i.e., any perturbation to the system decays to zero. When either of the linear damping terms is negative, the system is linearly unstable. For a single oscillator, the disturbance amplitude exponentially grows in time until it saturates to a limit cycle through the nonlinear terms. Similar behavior can occur for two oscillators, but other behaviors are also possible. For example, even though both eigenmodes are linearly unstable, they do not necessarily coexist at the limit cycle - one eigenmode can completely suppress the other, referred to as "quenching" [25]. This interaction/competition between two eigenmodes is a typical feature of nonlinear systems. For instance, when $\omega_1 = \omega_2$ and $\alpha_1 = \alpha_2 < 0$ in Eq. (1), nonlinearity of the form, $f_{NL,1} = -(a\eta_1^2 + \eta_2^2)\dot{\eta}_1$ and $f_{NL,2} = -(a\eta_2^2 + \eta_1^2)\dot{\eta}_2$, allows both modes to co-exist at the limit cycle for $a > 1$, while one mode drives the other to zero if $a < 1$.

Returning to the modeling of azimuthal modes, the azimuthal eigenmodes can be posed in several different ways: (1) as the nonlinear interaction and possibly competition between two standing eigenmodes (e.g., $\cos(n\theta)$ and $\sin(n\theta)$ where n is the azimuthal wavenumber), (2) as the interaction/competition between two counter-rotating eigenmodes (e.g., $\exp(in\theta)$ and $\exp(-in\theta)$), or (3) as a complex combination of standing and spinning modes, using a quaternion ansatz [26]. Depending on the choice of eigenmode pairs as well as the form of nonlinearity, both eigenmodes can coexist or one mode suppresses the other. In addition, the associated eigenvalues could be identical (degenerate) or different (non-degenerate) from each other, depending on the problem setup. For example, two standing modes could be non-degenerate through azimuthal non-uniformities in the system [27], while for two spinning modes, bulk azimuthal flow is a source of non-degeneracy [28].

The nonlinear interactions between these two azimuthal eigenmodes appear to first have been treated by Schuermans et al. [29], who considered a nominally axisymmetric system with degenerate eigenmodes. They examined the nonlinear interaction of two orthogonal standing modes of an azimuthal instability and showed that, when the system is linearly unstable, it evolves to a limit cycle where both standing modes coexist because of their degeneracy. The combination of two standing eigenmodes results in a single spinning wave, which could rotate in either the CW or CCW direction. The direction of the spinning wave is solely a function of initial conditions. Hummel et al. [30, 31] investigated a similar problem, posing it in the form of two counter-rotating eigenmodes, considering a nominally axisymmetric system, but allowing for non-degeneracy in the forms of different frequencies and/or growth rates of the CW and CCW eigenmodes. Similar to Schuermans's work, they showed that only spinning waves are present at limit cycle conditions, but also showed that non-degeneracy causes one spinning wave to be more probable than the other spinning wave. To summarize, these studies point to the fact that the nominally axisymmetric system shows only spinning wave dominant behavior at the limit cycle and, thus, the studies do not capture the fact that standing wave can also be present.

Noting this point, several studies have included the presence of non-uniformities in their models. Such non-uniformities can exist in geometry, flow, or flame, such as due to azimuthal variations in fuel-air ratio, swirl directions of individual nozzles, or a discrete number of nozzles distributed azimuthally. Noiray et al. [27] analyzed a non-degenerate combustor system due to

non-uniform flame-acoustic coupling and mean temperature distributions, and showed that two standing modes could coexist for weak non-uniformities, resulting in a spinning or mixed wave. For sufficiently large non-uniformities, only one standing mode survives. Which standing mode appears depends on the shape of non-uniformities. Later, Bauerheim et al. [28] considered a system with non-degeneracy due to non-uniformities as well as azimuthal bulk flow, and showed that non-uniformities promote standing waves, while azimuthal flow promotes spinning waves. A mixed wave could exist when both non-uniformities and azimuthal flow are present. Ghirardo et al. [32] considered a problem with degenerate eigenmodes and identical flames so that the azimuthal variation is due to the presence of discrete nozzles located azimuthally, and similarly showed co-existing standing/spinning waves, whose relative strengths are a function of nozzle spacing.

As noted earlier, experiments show the presence of erratic switching between standing and spinning waves at a fixed "steady-state" operational point. This switching may occur in three ways. First, consider the case where the deterministic model possesses one stable attractor associated with either standing or spinning wave. In this case, background noise perturbs the system continuously, allowing it to visit other points in the phase space, such as repelling or saddle point solutions. The associated joint probability density function (PDF) of amplitudes of two eigenmodes exhibits a unimodal distribution, roughly centered at the stable fixed point (FP). This type of model was first studied by Noiray and Schuermans [33], who introduced background noise effects by including stochastic additive forcing into their model. They showed how stochastic forcing manifests itself in a unimodal joint PDF of two standing mode amplitudes, which could be centered around standing or spinning wave-dominant behaviors, depending on the level of azimuthal non-uniformity. Second, the deterministic model could have multiple attractors. In the deterministic case, the system will remain on one attractor, based upon initial conditions. However, with sufficient noise levels, the system can travel between these multiple attractors. The joint PDF in this case exhibits multiple peaks in the distribution, associated with the different stable attractors [13, 18, 19]. For example, Faure-Beaulieu et al. [34] developed a background noise-driven model with non-uniform flame describing function, and found that the system can switch between two stable CCW/CW spinning attractors with a sufficient level of turbulent noise intensity. Similarly, Ghirardo and Juniper [35] developed a deterministic model that incorporated sensitivity of heat release to transverse velocity oscillations, and showed that the standing and spinning waves could be bistable at a fixed operating point, and thus, the system could intermittently switch between them due to background noise. Thirdly, parametric noise can qualitatively change system dynamics, stabilizing or destabilizing attractors for sufficient parametric noise. For instance, Bothien et al. [36] noted that the preference of standing or spinning wave is very sensitive to azimuthal flame temperature non-uniformity. Thus, the parametric noise would be expected to lead to intermittency between standing and spinning waves at a fixed operating condition. In any of these cases, it is clear that the inherent background noise that is present in combustion systems plays an important role in the system's dynamics.

Another interesting point about azimuthal modes is the behavior of the nodal line during the limit cycle. As noted earlier, in a system with azimuthal symmetry, there is no reason for the nodal line to remain fixed during azimuthal mode oscillations, in contrast to axial/radial mode oscillations. For example, large eddy simulations have shown that the nodal line of the standing wave slowly rotates at a mean swirl velocity [20, 21]. Similarly, the experimental study by Vignat et al. [37] reported the nodal line moving in a seemingly random fashion. However, the system's non-uniformities can fix the nodal line at a certain azimuthal location as shown in the experiments

[15] as well as reduced order models [34, 38]. In addition, the deterministic motion of the nodal line has been observed. Experimental studies from Kim et al. [39, 40] and Worth et al. [13] showed that the nodal line periodically oscillates around a fixed azimuthal location with a slow time scale. In other words, the nodal line's average location appeared to be fixed, but it did oscillate about this point in an approximately sinusoidal, coherent fashion; i.e., not randomly. These oscillations lead to modulations in pressure amplitude measured at a fixed azimuthal position. Furthermore, Kim et al. [39] and Indlekofer et al. [41] showed that (anti-) nodal line oscillations are coupled with oscillations of spinning wave direction.

We note in closing an additional point around modeling nonlinear systems with two closely spaced frequencies, which introduce an additional slow time scale, $1/(\omega_1 - \omega_2)$, and, therefore additional terms when applying the method of averaging techniques for nonlinear oscillator dynamics. These additional terms have not been applied in most studies of nonlinear azimuthal modal dynamics [27, 30, 33], but as noted by Acharya et al. [42], they can incorporate additional sensitivities to frequency spacing, as well as influence limit cycle amplitudes and their stability. In extending this work to noise-driven systems, John et al. [43] similarly noted how these additional slow time scale terms led to drift in phase-space trajectories.

To summarize the findings of reduced order models, azimuthal modes exhibit a purely spinning wave during the limit cycle if the system is axisymmetric. The spinning direction depends on initial conditions, but non-degeneracy causes the system to prefer one direction over the other. In systems with azimuthal non-uniformity, the system may show a mixed or standing wave, and the orientation of the nodal line relies on the shape of the non-uniformity. Lastly, background noise may be responsible for switching between CW and CCW spinning directions as well as standing and spinning waves.

The first major objective of this paper is to present data from a high Reynolds number industrial-scale facility, where a variety of behaviors - standing, spinning, and intermittent behaviors - are observed in a single facility, enabled by systematically varying power and azimuthal fuel staging. The second key objective is to develop a low order model of thermoacoustic azimuthal modes. While previous models capture some of the aforementioned effects, the main contribution of this paper is to present a comprehensive framework that includes all of the effects. This paper is related to recent work by Faure-Beaulieu et al. [44] which utilized the quaternion ansatz [26, 45] referenced earlier; we will compare results from that study to those from the present analysis, which formulates the problem as a superposition of two standing eigenmodes.

2. Experiment Overview

2.1 Experimental facility

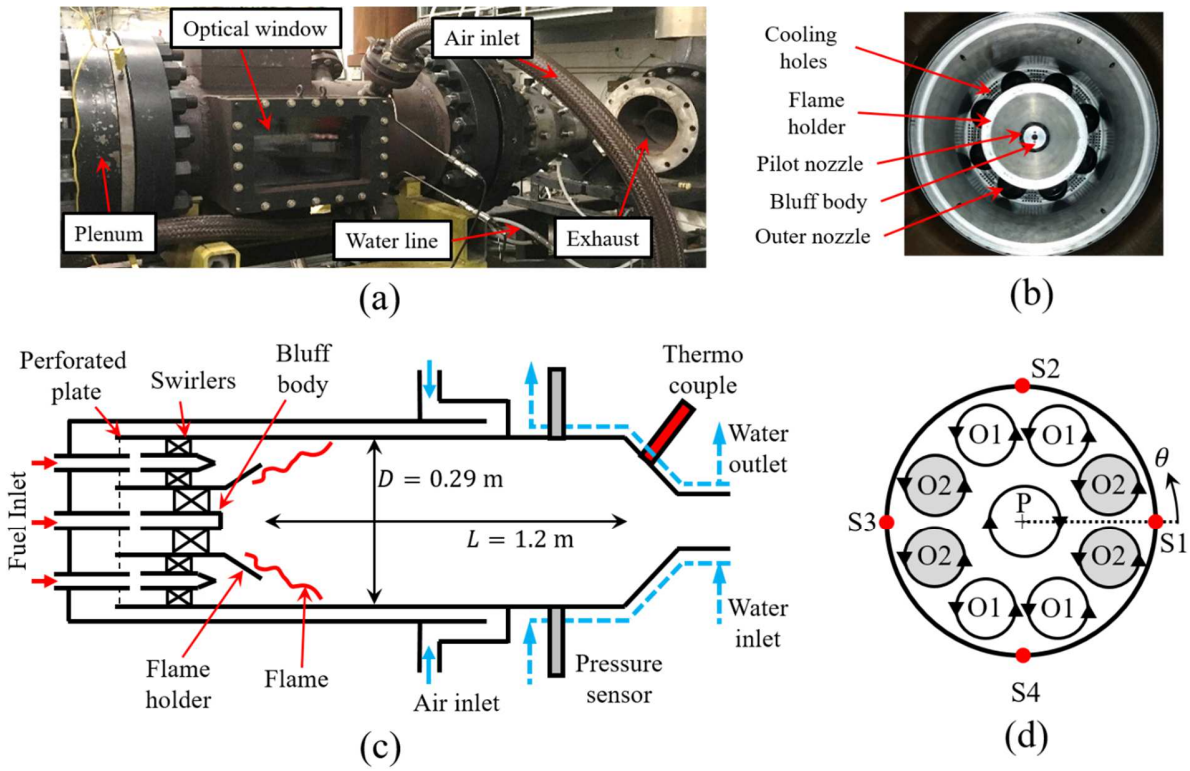

Fig. 1. (a) Experimental facility (b) Nozzle front view (c) Side schematic of combustor (d) Schematic of the nozzle. Red dots indicate each sensor location.

This section briefly introduces the experimental facility, consisting of a multi-nozzle can combustor; more details can be found in [39]. Figure 1(a) and (c) show a side view of the combustor used in this study. Air from four inlets enters near the axial midpoint of the rig and flows through an annular section in the upstream direction, cooling the chamber wall. At the front of the test article, the preheated air mixes with natural gas, passes through each nozzle, and the mixture is combusted near the flame holder. The product accelerates near the downstream contraction area and exits the system through the water-cooled exhaust. Figure 1(b) and (d) represent multiple nozzles and fuel staging configurations. The nozzle consists of 8 outer nozzles ('O') and a center pilot nozzle ('P'). The swirl directions for pilot and outer nozzles are CW and CCW, respectively. The outer nozzles have two separate fuel lines, denoted as 'O1' and 'O2'. Radial flame/temperatures asymmetry is controlled by the pilot ratio, $PR = \dot{m}_P/(\dot{m}_P + \dot{m}_O)$ where $\dot{m}_P$ and $\dot{m}_O$ are the fuel flow rate through the pilot and outer nozzles, respectively. Similarly, azimuthal asymmetry in flame/temperature is controlled by the fuel split between O1 and O2, quantified by an outer ratio, $OR = \dot{m}_{O2}/(\dot{m}_{O1} + \dot{m}_{O2})$, e.g., $OR = 0.5$ means uniform fuel distribution in the azimuthal direction. Overall combustor flow rate is used as a control parameter for thermal power. Preheat temperature and global equivalence ratio are maintained constant. Acoustic pressure is measured with four pressure transducers (6021A Kistler) flush-mounted in the chamber at equidistance azimuthal positions (Fig. 1(d)).

2.2 Post-Processing

The measured acoustic pressure time series is band-pass filtered with a bandwidth of 60

HZ at around the peak frequency corresponding to the first azimuthal mode. This filtered signal is modeled as a superposition of CCW and CW waves.

$$\begin{aligned}\hat{p}(\theta,t) &= f(\tau)e^{i(n\theta-\omega_F(\tau)t)} + g(\tau)e^{-i(n\theta+\omega_G(\tau)t)} \\ &= F(\tau)e^{i(n\theta+\varphi_F(\tau)-\bar{\omega}_{FG}t)} + G(\tau)e^{-i(n\theta-\varphi_G(\tau)+\bar{\omega}_{FG}t)}\end{aligned} \tag{2}$$

Here, $\hat{p}$ is a filtered signal, n azimuthal wavenumber, f and g are slowly time-varying amplitudes of CCW/CW waves, ω_F and ω_G are angular frequencies of each wave, $F$and $G$are magnitudes of each wave, φ_F and $\varphi_G$are phases of each wave, $\bar{\omega}_{FG}$ is an averaged angular frequency, and τ is a "slow" time scale relative to the acoustic time scale, i.e., $\tau = \epsilon t$ where $\epsilon \ll 1$.

A spin ratio (SR), which quantifies the dominant mode between standing and spinning waves, is defined as [46]

$$SR(\tau) = \frac{F(\tau) - G(\tau)}{F(\tau) + G(\tau)}. \tag{3}$$

$SR = 0$ means a purely standing wave, $SR = \pm 1$ a purely spinning wave in CW$(-)$ or CCW$(+)$ direction. Otherwise, the mode is a combination of standing and spinning waves, i.e., a mixed wave. The presence of noise in these modal amplitudes introduces bias errors in the SR estimate, whose magnitude was estimated from Monte Carlo simulations and quantified in subsequent sections, using an approach that is detailed in Appendix A.

Next, the absolute value of $\hat{p}$ provides a pressure magnitude at θ.

$$|\hat{p}(\theta,\tau)| = \left[F(\tau)^2 + G(\tau)^2 + 2F(\tau)G(\tau)\cos\left(2n\theta + \varphi_{FG}(\tau)\right)\right]^{1/2} \tag{4}$$

Here, $\varphi_{FG} = \varphi_F - \varphi_G$ is the phase difference between CCW/CW waves. The location of the maximum pressure magnitude, also referred to as the anti-nodal line, is then given by

$$\theta_a(\tau) = \frac{2k\pi - \varphi_{FG}(\tau)}{2n}, \qquad \text{where} \qquad k = 0, 1, 2, \ldots \tag{5}$$

The magnitude at the anti-node is

$$|\hat{p}(\theta_a,\tau)| = F(\tau) + G(\tau). \tag{6}$$

The quantities, F, G, SR, φ_{FG}, and $|\hat{p}(\theta_a)|$ are extracted from the filtered signal using a least squares fit and used to describe the modal dynamics of the azimuthal mode [39].

2.3 Experimental observations

In this section, we will first examine the uniform fuel staging at three different operating conditions (case 1 - 3), which are summarized in Table 1. Next, the comparison between uniform and non-uniform fuel staging will be introduced.

Table 1 Operating conditions for each case

Case	Preheat temp. (K)	Equiv. ratio (-)	PR (-)	OR (-)	Air mass flow (kg/s)
1	600	0.55	0.1	0.5	1.2
2	600	0.55	0.1	0.5	1.4
3	600	0.55	0.1	0.5	1.54

2.3.1 Uniform fuel staging

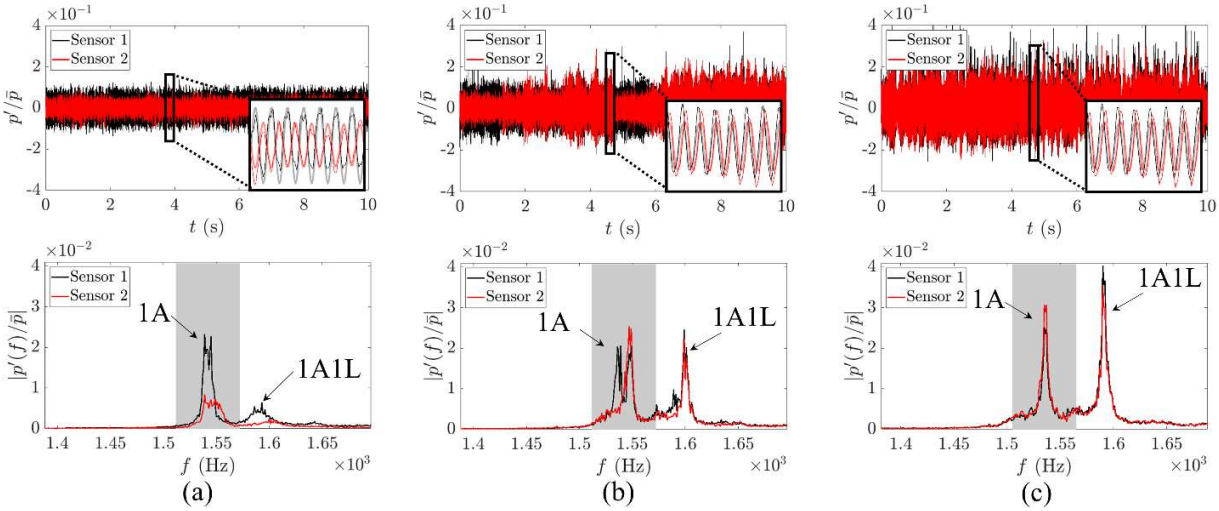

Fig. 2. Top: raw pressure signals from sensors 1 and 2 for (a) case 1, (b) 2, and (c) 3. In subfigures, thick and thin lines denote the band-pass filtered and raw signals, respectively. Bottom: ensemble-averaged Fourier transform from sensors 1 and 2 for each case.

The first row of Fig. 2(a) – (c) shows 10 seconds time trace of the raw pressure signals measured from two sensors, S1 and S2, for cases 1 – 3. S3 and S4 are omitted here, as they are similar to S1 and S2, respectively. The bottom of Fig. 2(a) – (c) illustrates the ensemble-averaged magnitudes of the Fourier transform, which is obtained by estimating the Fourier transform for 1 second of data, averaging the power spectrum, and then taking the square root of the averaged value. The figures show several distinct peaks. The two dominant ones are labeled 1A (first azimuthal) and 1A1L (first azimuthal-first longitudinal) [47], whose frequency difference is about 53 Hz. This study focuses on 1A mode only, i.e., the signal is band-pass filtered around 1A with a bandwidth indicated by the shaded region.

As shown in Fig. 2(a), when the flow rate is low (case 1), the pressure amplitude for S1 is larger than that for S2, but they are almost out-of-phase, implying that the mode is close to a standing wave. In addition, one can see that the 1A mode in the spectrum consists of two very closely spaced peaks, approximately 6 Hz apart, which will be discussed later.

For an intermediate flow rate (case 2), the relative amplitude changes in time, i.e., sometimes S1 has a larger amplitude than S2; other times they have similar amplitudes. The spectrum also shows two closely spaced peaks 11 Hz apart, which is higher than case 1.

For a high flow rate (case 3), the amplitudes remain similar to each other all the time, and the spectrum is composed of only a single peak.

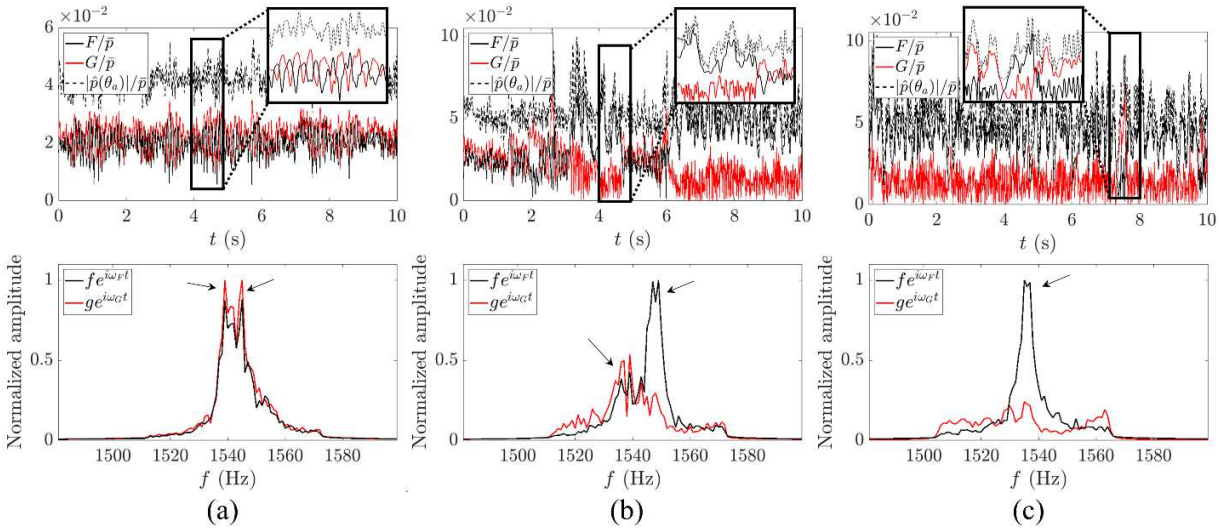

Fig. 3. Top: time trace of CCW(F)/CW(G) wave magnitudes as well as the pressure anti-node magnitude for (a) case 1, (b) 2, and (c) 3. Bottom: ensemble-averaged Fourier transform of CCW/CW waves for each case, normalized by their peak value.

We next consider the slow time scale characteristics of the extracted parameters. The top of Fig. 3(a) – (c) illustrates the time trace of extracted CCW/CW wave magnitudes normalized by static pressure, and the normalized pressure magnitude at the instantaneous anti-node for each case. The bottom of Fig. 3(a) – (c) plots the ensemble-averaged Fourier transform of CCW/CW waves for each case.

For case 1, F and G are oscillating around a fixed value, but their oscillations are approximately sinusoidal and out-of-phase to each other. The corresponding Fourier transform shows two peaks closely spaced to each other where their difference is about 6 Hz. Bulk azimuthal flow is one potential mechanism for this frequency difference. Indeed, CFD calculations, not shown here, indicate that there is a net CCW bulk azimuthal flow, the result from competing between the outer (CCW) and inner (CW) swirl, that could lead to a frequency difference of up to 10 Hz. If this were the mechanism for these two peaks, however, the CW and CCW waves would separately peak at one of the two frequencies. However, Fig. 3(a) clearly shows that each of the CCW/CW waves has two peaks overlapping each other. We will show later that these two peaks are a manifestation of a quasi-periodic oscillation, where the instantaneous amplitudes, F and G, oscillate at the frequency difference.

For case 2, F and G show intermittency as they sometimes show standing wave behavior observed in case 1; other times F dominates over G. The Fourier transform also exhibits two peaks: the first peak where CCW/CW waves have similar amplitudes, the second peak where CCW amplitude is greater than CW amplitude.

For case 3, F dominates over G most of the time, which is also seen in the Fourier transform.

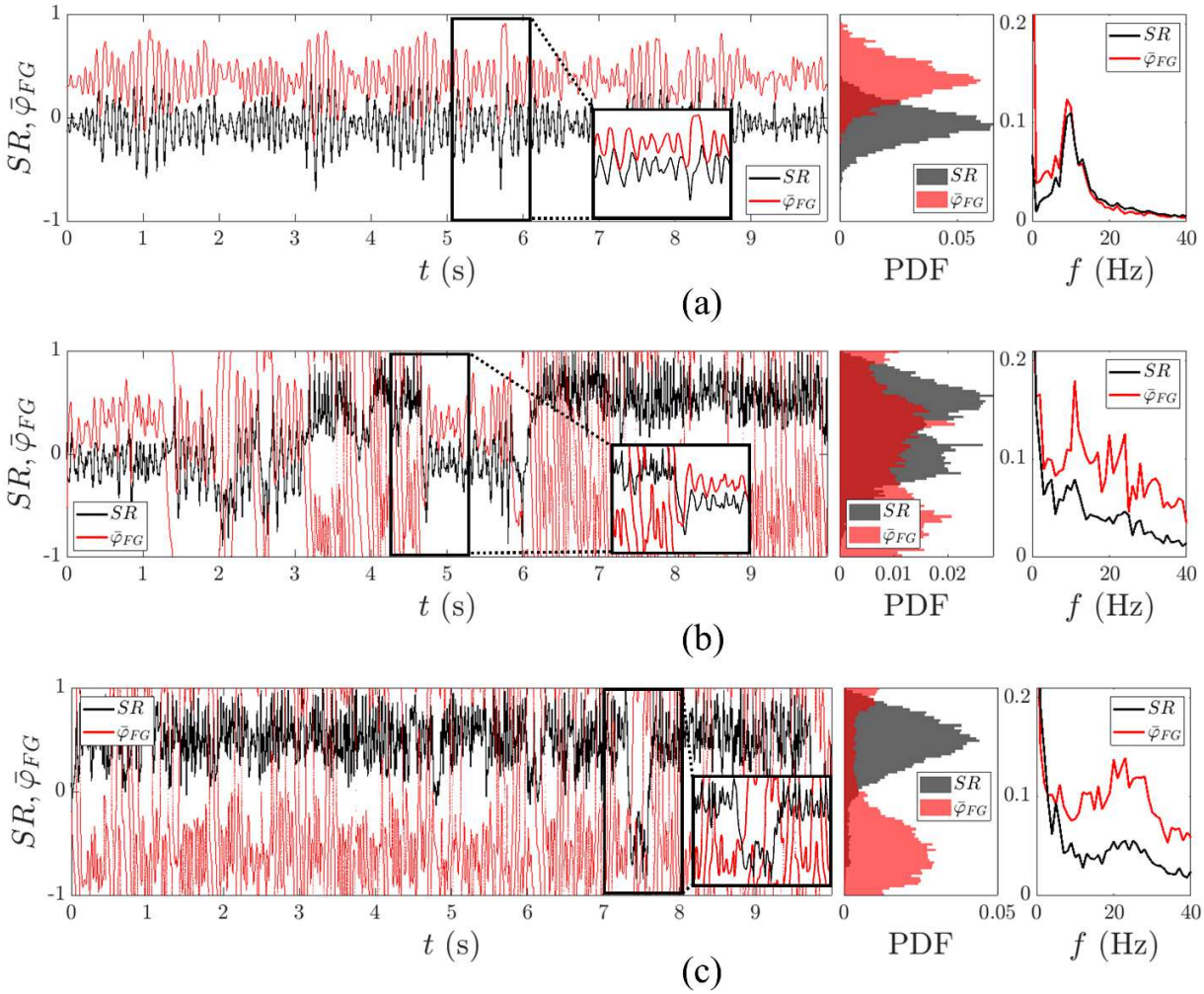

Fig. 4. SR and $\bar{\varphi}_{FG}$ in time series (left), their PDF (middle), and ensemble-averaged Fourier transform (right) for (a) case 1, (b) 2, and (c) 3.

Figure 4 plots the time trace of SR and the normalized phase difference, $\bar{\varphi}_{FG} = \varphi_{FG}/\pi$, between CCW/CW waves, their PDFs, and the ensemble-averaged Fourier transform for each case. For case 1, two interesting observations can be made. First, SR and $\bar{\varphi}_{FG}$ periodically oscillate around zero and 0.4, respectively. We refer to this as a quasi-periodic standing wave. These periodic oscillations are clearly evident in the Fourier transform of SR and $\bar{\varphi}_{FG}$. Second, the oscillation in $\bar{\varphi}_{FG}$ leads SR by about 90°. These observations imply that they are not driven by simply a stochastic forcing, but rather coupled to each other by a lower degree of freedom process.

For case 2, SR and $\bar{\varphi}_{FG}$ exhibit intermittency, switching between two values. Notice that the abrupt transitions in SR and $\bar{\varphi}_{FG}$ are synchronized, i.e., when SR switches from zero to 0.55, $\bar{\varphi}_{FG}$ shifts from 0.4 to -0.7, and vice versa. A bimodal distribution in the PDF implies the existence of two stable FPs in the system.

For case 3, SR and $\bar{\varphi}_{FG}$ mostly linger around nearly fixed values of 0.55 and -0.7, respectively, indicating that the system has one stable equilibrium point. This is confirmed by a unimodal distribution in the PDF. As discussed in Appendix A, the SR estimate is subject to bias

errors, which can influence the interpretation of estimated SR values. Using the approach described there to estimate this bias error leads to an estimated bias of 0.1 ± 0.05. As such, we can confidently say that this $SR = 0.55$ value reflects a mixed wave, not a purely spinning wave with large noise intensity. SR transitions to -0.55 at $t = 7.5$ s, but it immediately returns to 0.55. Also note that the Fourier transforms for case 3 show no dominant peak compared to case 1.

To eliminate the high dimensional (turbulent) dynamics and visualize the low order dynamics, a phase averaging technique, detailed in [39], was applied to each case. The basic idea is to determine the average evolution of system quantities - we will demonstrate the idea here on SR and $\bar{\varphi}_{FG}$ space. In other words, this procedure determines the average behavior of SR and $\bar{\varphi}_{FG}$ after time, Δt. When plotted in this way, limit cycles and quasi-periodic oscillations appear as FPs and closed orbits, respectively, in phase space (while, theoretically, quasi-periodic orbits are never closed, the averaging procedure necessarily has finite phase space resolution and closes them).

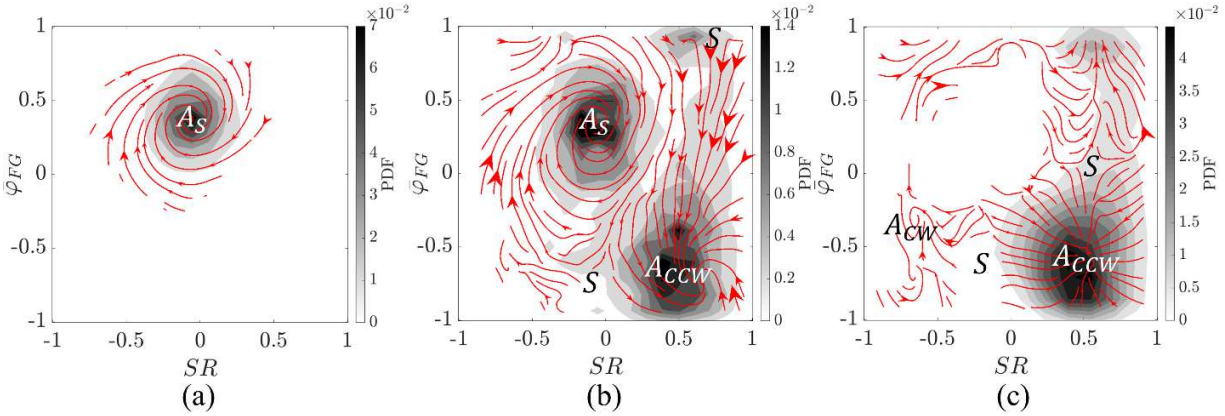

Fig. 5. Average phase portrait in SR and $\bar{\varphi}_{FG}$ space for (a) case 1, (b) 2, and (c) 3. The grayscale denotes the joint PDF of SR and $\bar{\varphi}_{FG}$. The red arrows and their head size indicate the trajectories and velocity magnitude.

Figure 5 shows the $(SR, \bar{\varphi}_{FG})$ phase portraits for cases 1 - 3. Note that the top and bottom boundaries are connected because of the periodicity of $\bar{\varphi}_{FG}$. For case 1, the phase portrait shows the trajectories converging to the center, $(SR, \bar{\varphi}_{FG}) = (0, 0.4)$, and the joint PDF shows a unimodal distribution. This implies that the system has one stable attractor at the center, denoted by A_S where subscript 'S' indicates a standing wave. In addition, the trajectories are spiraling in towards the attractor in the CW direction, which is expected from the 90° phase lag between the oscillations in SR and $\bar{\varphi}_{FG}$ described in Fig. 4(a). Without the noise contribution, the system would be stabilized at the stable attractor. However, the noise continuously perturbs the system from its attractor, and the system repeatedly converges towards this attractor, forming the CW spiral trajectories.

For case 2, a much larger range of behaviors and attractors are observed and the structure of the phase portrait is more complex. First, the stable attractor at $(0, 0.4)$ observed from case 1 still exists, but the system shows another stable attractor at $(0.55, -0.7)$, denoted by A_{CCW}, which corresponds to the CCW dominant mixed wave. The joint PDF similarly demonstrates discrete peaks associated with these two attractors at $(0, 0.4)$ and $(0.55, -0.7)$. Second, two saddle points, denoted by S, are also observed near the top and bottom boundaries.

For case 3, A_{CCW} still exists at the bottom right corner, but A_S is not visible, demonstrating that it is strongly repelling. Rather, a CW mixed wave attractor, A_{CW}, appears at the bottom left

corner although the joint PDF around it is sparse. This implies that A_{CW} may be a stable attractor, but its strength is so weak that the system can be readily expelled from the attractor by the external noise, and it converges to A_{CCW}. The system stays around this attractor most of the time.

Figure 5 shows the overall structure of the phase portrait. However, there exists an empty region in the portrait because of either insufficient sampling time or low noise intensity. We have acquired additional phase portraits with longer sampling time at a range of other operating conditions in Appendix B [39]. These portraits show that there is a saddle point in the empty region in Fig. 5, but the overall structure remains the same even at different operating conditions.

2.3.2 Effects of non-uniform fuels staging

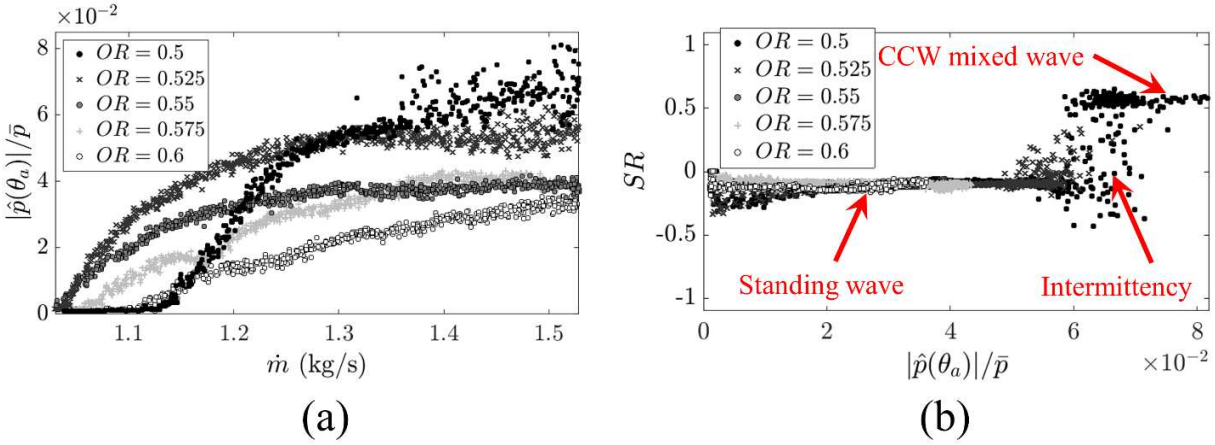

Fig. 6. (a) Normalized pressure anti-node magnitude as a function of air mass flow rate with different ORs. (b) SR as a function of normalized pressure anti-node magnitude with different ORs.

Figure 6(a) represents the normalized anti-node magnitude, $(F+G)/\bar{p}$, with respect to air mass flow rate with different ORs. The magnitude exhibits a supercritical Hopf bifurcation at a certain mass flow rate, at which it exhibits oscillations at 1A mode. The magnitude increases monotonically with mass flow rates over the range tested here. As shown in the figure, both the location of the Hopf bifurcation and magnitudes are also functions of the azimuthal non-uniformity parameter, OR.

Figure 6(b) illustrates SR as a function of anti-node magnitude with different ORs. The SR in this plot is the averaged value over 1 second. Starting from $OR = 0.5$, SR is close to zero at low magnitudes, implying a standing wave. For intermediate magnitudes, SR fluctuates between zero and 0.55, demonstrating intermittency. For high amplitudes, SR is stabilized at 0.55, i.e., CCW mixed wave. When $OR > 0.5$, the magnitude is too low to reach the bistable regime, resulting in a standing wave only. Although not shown, the time trace of SR and $\bar{\varphi}_{FG}$ and their phase portraits are similar to those in Fig. 4(a) and Fig. 5(a), except that $\bar{\varphi}_{FG}$ oscillates around zero for non-uniform fuel staging. The interested reader can refer to [40].

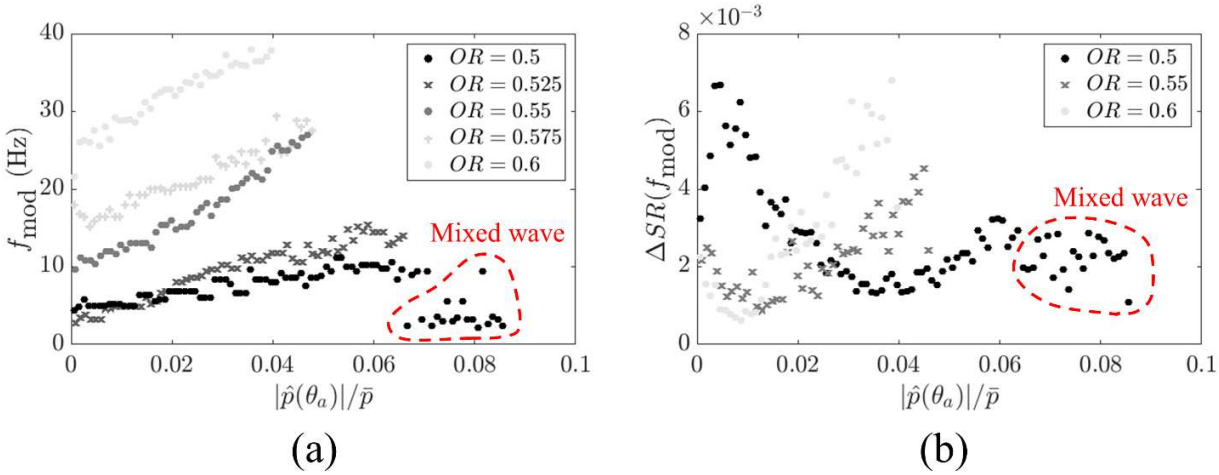

(a) (b)

Fig. 7. (a) SR modulation frequency as a function of normalized anti-node magnitude with different OR s. (b) SR modulation amplitude as a function of normalized anti-node magnitude with different ORs.

We observed in Fig. 4(a) that the SR oscillates at a certain frequency, f_{mod}, and the associated peak amplitude, $\Delta SR(f_{\mathrm{mod}})$. Thus, it is worthwhile to explore their response to thermal power/azimuthal fuel staging. As the instability amplitude is monotonically related to overall combustor power/flow rate for this investigated parameter range (but certainly not in general), these dependencies more probably reflect a sensitivity of this quasi-periodic standing wave to linear amplification/damping parameters (as also suggested by the theory described in the next section) that influence combustion instability amplitude. As such, we plot the modulation frequency and the associated amplitude as a function of anti-node magnitude at different ORs in Fig. 7. Figure 7(a) shows that the modulation frequency increases with the anti-node magnitude as long as the azimuthal mode remains as a standing wave. In addition, the modulation frequency increases with azimuthal non-uniformity. Figure 7(b) shows that as the anti-node magnitude increases, the modulation amplitude first decreases and then increases. The reason for these trends is detailed in Appendix C.

To sum up the overall observations, the system with uniform fuel distribution exhibits a standing wave at low flow rates, intermittency between standing and mixed waves at intermediate flow rates, and CCW mixed wave at high flow rates. When the fuel is staged non-uniformly, the system exhibits only the standing wave FP regardless of mass flow rates. Figure 19 in Appendix D summarizes these results, showing them in two different ways. The cloud of points in the images represents the experimental conditions that this plot is based upon.

3. Modeling - Formulation

This section derives the governing equations that describe the azimuthal modal dynamics. This approach closely follows the procedure used in prior studies – namely, assuming linear acoustics with nonlinear source terms, using a Galerkin expansion to decompose the nonlinear partial differential equation into a system of nonlinear, coupled ordinary differential equations [27, 30, 33]. The resulting equations are then temporally averaged over the fast acoustic time scale, following the Krylov-Bogoliubov method [48], leaving nonlinear coupled equations for the slow time scale evolution of the disturbance amplitude and phase difference. The key contribution of

this section is incorporating all the effects noted into Introduction in a rigorous, unified fashion.

3.1 Governing equations

This section briefly summarizes the development of the stochastic, nonlinear wave equation, presented below, closely following prior studies, [27, 49].

$$\frac{\partial^2 p}{\partial t^2} - \frac{c^2}{R^2}\frac{\partial^2 p}{\partial \theta^2} = h_1\left(p, \frac{dp}{dt}\right) + \xi_1(t) + h_2\left(p, \frac{dp}{dt}\right)\xi_2(t) \tag{7}$$

Here, p is the acoustic pressure, c the sound speed, R the chamber radius, ξ_1 an additive background noise term, ξ_2 a parametric noise term, and $h_{1,2}$ represent all other source/sink and wave propagation terms due to unsteady heat release, temperature non-uniformity, bulk flow effects, and nonlinearities [49]. Notice that the wave equation has been spatially integrated into the axial and radial directions, and that mean flow, density gradient, and losses at boundaries are encapsulated in these general functions, $h_{1,2}$.

Note that the solutions of the homogeneous wave equation, given by:

$$p(\theta, t) = \sum_{m=1}^{\infty}\left[\eta_{1,m}(t)\cos(m\theta) + \eta_{2,m}(t)\sin(m\theta)\right] \tag{8}$$

constitute a complete, orthogonal set of basis functions. As such, the essence of the Galerkin method is to use these basis functions for writing the solution of the more general, nonlinear Eq. (7). There is no approximation when the infinite summation is retained, but truncation necessarily introduces approximations. We will truncate this summation as a single mode that nonlinearly interacts with itself. Nonlinear interactions between multiple modes are essential to include for cases where gas dynamical nonlinearities are important, but these types of nonlinearities are negligible in the "low" acoustic amplitudes typically observed in lean premixed systems (e.g., Fig. 6(a) shows $(F+G)/\bar{p}$ levels of maximum 8%) [50, 51]. Furthermore, the heat release nonlinearities, which generally dominate nonlinear effects in lean premixed systems, lead to strong self-interactions of a mode with itself [52-54]. Thus, we shall approximate the acoustic pressure associated with a given n^{th} eigenmode as [27]

$$p(\theta, t) \approx \eta_1(t)\cos(n\theta) + \eta_2(t)\sin(n\theta) \tag{9}$$

where η_1 and η_2 are the amplitudes of two orthogonal (horizontal and vertical) standing modes of azimuthal wavenumber, n. The subscript, n, in η has been omitted here.

Next, we can treat the function h_1 in Eq. (7) quite generally by expanding it as a Taylor series [55] truncated at fourth order:

$$\begin{aligned} h_1\left(p, \frac{dp}{dt}\right) = {} & B_{00}(\theta) + B_{10}(\theta)p + B_{01}(\theta)\dot{p} + B_{20}(\theta)p^2 + B_{11}(\theta)p\dot{p} + B_{02}(\theta)\dot{p}^2 \\ & + B_{30}(\theta)p^3 + B_{21}(\theta)p^2\dot{p} + B_{12}(\theta)p\dot{p}^2 + B_{03}(\theta)\dot{p}^3 + B_{40}(\theta)p^4 \\ & + B_{31}(\theta)p^3\dot{p} + B_{22}(\theta)p^2\dot{p}^2 + B_{13}(\theta)p\dot{p}^3 + B_{04}(\theta)\dot{p}^4 \end{aligned} \tag{10}$$

where $\dot{p}$ is the time derivative of p, and B_{ij}'s are coefficients of $p^i\dot{p}^j$. Note that in previous studies,

$h_1(p,\dot{p})$ was often considered as the time derivative of heat release fluctuation, $d\dot{Q}/dt$, where $\dot{Q}(p)$ is a function of pressure only [27, 30]. This approach, however, cannot capture some of the terms in Eq. (10) (e.g., $B_{10}p$ and $B_{12}p\dot{p}^2$) that will be shown to introduce important qualitative features in the modal dynamics. The coefficients B_{ij} are non-time varying but can vary azimuthally; physically this would occur because of discrete nozzle locations, azimuthally non-uniform temperature distribution, azimuthally non-uniform thermo-acoustic coupling strength, etc. In order to account for this in a general fashion, we write them as the following series:

$$\begin{aligned} B_{01}(\theta) &= -\alpha + \underbrace{\beta\left(1+\sum_{m=1}^{\infty} C_{m,01}\cos(m\theta)+\sum_{m=1}^{\infty} S_{m,01}\sin(m\theta)\right)}_{=\beta_0(\theta)} \\ B_{ij}(\theta) &= b_{ij}\left(1+\sum_{m=1}^{\infty} C_{m,ij}\cos(m\theta)+\sum_{m=1}^{\infty} S_{m,ij}\sin(m\theta)\right) \;\; for\; i\neq 0, j\neq 1 \end{aligned} \tag{11}$$

Although not necessary, it is convenient to decompose the linear growth/damping term, B_{01}, into a linear damping term, α, which is not dependent on θ, and the linear growth term, $\beta_0(\theta)$, which is a function of θ [27]. Note that α and β in Eq. (11) coincide with the linear damping (α) and gain (β) in [44].

We next follow the standard steps in the Galerkin expansion approach - substitute Eq. (9), (10), and (11) into Eq. (7), multiply both sides by $\cos(n\theta)$ or $\sin(n\theta)$, and integrate these equations from 0 to 2π with respect to θ, producing two sets of second order differential equations,

$$\begin{aligned} &\ddot{\eta}_1+\left(\alpha-\beta\left(1+\frac{C_{2n,01}}{2}\right)\right)\dot{\eta}_1+\omega_1^2\eta_1 \\ &\qquad = f_1(\eta_1,\eta_2,\dot{\eta}_1,\dot{\eta}_2)+\zeta(t)+\int_0^{2\pi} h_2(\eta_1,\eta_2,\dot{\eta}_1,\dot{\eta}_2)\sin(n\theta)\,\xi_2(t)\,d\theta \\ &\ddot{\eta}_2+\left(\alpha-\beta\left(1+\frac{C_{2n,01}}{2}\right)\right)\dot{\eta}_2+\omega_2^2\eta_2 \\ &\qquad = f_2(\eta_1,\eta_2,\dot{\eta}_1,\dot{\eta}_2)+\zeta(t)+\int_0^{2\pi} h_2(\eta_1,\eta_2,\dot{\eta}_1,\dot{\eta}_2)\cos(n\theta)\,\xi_2(t)\,d\theta \end{aligned} \tag{12}$$

where

$$\omega = nc/R,\;\; \omega_1^2=\omega^2-b_{10}\left(1+C_{2n,10}/2\right),\qquad \omega_2^2=\omega^2-b_{10}\left(1-C_{2n,10}/2\right) \tag{13}$$

The detailed derivation and the explicit expressions for f_1 and f_2 are shown in Appendix E. Here, $\zeta(t)$ is a spatially averaged additive noise source. Equation (12) describes the 2nd order harmonic oscillators of two orthogonal standing eigenmodes coupled through the source terms. Note that even order nonlinearities (e.g., terms multiplied by b_{20}, b_{11}, and b_{40}, etc) are eliminated during the spatial averaging, i.e., only the odd order terms survive [30]. Similarly, azimuthal non-uniformity terms higher than $4n$ order are averaged out, and only $2n$ and $4n$ terms have an impact on the dynamics [27]. For the first azimuthal mode ($n=1$), for example, only terms multiplied by

$C_2, S_2, C_4,$ and S_4 remain. In other words, the C_8 and S_8 terms, which would be nonzero for the eight outer nozzle configuration used in this experimental facility, have no impact on the first azimuthal mode. This is due to the truncation at fourth order in Eq. (10), e.g., if truncated at sixth order, Eq. (12) would contain the non-uniformity terms up to $6n$. Moreover, since the dominant nonuniform coefficient in the fuel staging configuration (Fig. 1(d)) is C_2, only the first azimuthal mode can be influenced by varying OR.

Next, Eq. (13) shows that the frequency difference, $\Delta\omega = \omega_2 - \omega_1$, and $C_{2n,01}$ are correlated, i.e., if $|C_{2n,01}|$ gets larger, $|\Delta\omega|$ will as well. This explains the reason for higher modulation frequency with higher OR at a fixed instability amplitude in Fig. 7(a). However, the sign of the correlation depends on the sign of b_{10}. Physical arguments suggest that $b_{10} < 0$; for the first azimuthal mode ($n = 1$), if $C_{2,01} > 0$, then the temperature (or speed of sound) distribution in the horizontal direction would be higher than that in the vertical direction, giving rise to $\omega_1 > \omega_2$, or equivalently, $\Delta\omega < 0$.

3.2 Averaged equations

Given the fact that $\eta_{1,2}(t)$ are oscillating harmonically with a temporally varying amplitude and phase, it is convenient to utilize a Van der Pol decomposition to rewrite the temporal dynamics [56].

$$\begin{aligned}\eta_1(t) &= A(\tau)\cos\big(\omega_1(\tau)t + \phi_A(\tau)\big) = A(\tau)\cos\big(\bar{\omega}t + \varphi_A(\tau)\big)\\ \eta_2(t) &= B(\tau)\cos\big(\omega_2(\tau)t + \phi_B(\tau)\big) = B(\tau)\cos\big(\bar{\omega}t + \varphi_B(\tau)\big)\end{aligned} \tag{14}$$

where

$$\begin{aligned}&\bar{\omega} = \frac{\omega_1(\tau) + \omega_2(\tau)}{2}, \quad \Delta\omega = \omega_2(\tau) - \omega_1(\tau),\\ &\varphi_A(\tau) = \phi_A(\tau) - \frac{\Delta\omega t}{2}, \quad \varphi_B(\tau) = \phi_B(\tau) + \frac{\Delta\omega t}{2}\end{aligned} \tag{15}$$

We assume that the characteristic time scales over which the amplitudes and phase ($A,\ B$ and φ, respectively) vary are much slower than the acoustic time scale, i.e., $\tau = \epsilon/\bar{\omega}$. Assuming $\zeta(t)$ in Eq. (12) is Gaussian white noise, one can perform deterministic and stochastic averaging [48, 57-59] to produce the following first order differential equations for the slowly varying amplitudes and phase:

$$\begin{aligned}\frac{dA}{d\tilde{t}} &= f_A\big(A, B, \varphi; \Delta, C_{2,ij}, S_{2,ij}, C_{4,ij}, S_{4,ij}\big) + \frac{\Gamma}{4\bar{\omega}^3 A} + \frac{\zeta_A}{\bar{\omega}}\\ \frac{dB}{d\tilde{t}} &= f_B\big(A, B, \varphi; \Delta, C_{2,ij}, S_{2,ij}, C_{4,ij}, S_{4,ij}\big) + \frac{\Gamma}{4\bar{\omega}^3 B} + \frac{\zeta_B}{\bar{\omega}}\\ \frac{d\varphi}{d\tilde{t}} &= f_{\varphi}(A, B, \varphi; \Delta, C_{2,ij}, S_{2,ij}, C_{4,ij}, S_{4,ij}) + \left(\frac{1}{A} + \frac{1}{B}\right)\frac{\zeta_\varphi}{\bar{\omega}}\end{aligned} \tag{16}$$

where $\varphi = \varphi_B - \varphi_A$, $\Delta = \Delta\omega/\bar{\omega}$, $\tilde{\alpha} = \bar{\omega}\alpha, \tilde{\beta} = \bar{\omega}\beta, \tilde{b}_{ij} = \bar{\omega}^{2-j} b_{ij}, \tilde{t} = \bar{\omega}t$, and ζ_A, ζ_B, and ζ_φ are uncorrelated white noises of intensity $\Gamma/2\bar{\omega}^2$. The detailed expressions for $f_{A,B,\varphi}$ are described in Appendix F. Here, the n in the subscript of C_{ij} and S_{ij} has been dropped. Also notice that the parametric noise term has been neglected for simplicity, i.e., $\xi_2(t) = 0$. The effect of this term

will be numerically considered later. Equation (16) describes the amplitudes and phase difference dynamics of the second order coupled oscillators in Eq. (12). These equations are a quite general representation of the modal dynamics, and serve as a useful point of departure for a range of different types of analyses. For example, referring back to the discussion in the Introduction, azimuthal non-uniformity effects are parameterized by C_{ij} and S_{ij}, nondegeneracy by C_{ij}, S_{ij}, and Δ, nonlinearities by $\tilde{b}_{ij}$, and background noise by Γ. In subsequent sections, we will consider the deterministic FP solutions of a simplified version of these equations, the stability of those FPs, and the bifurcation point.

4. Illustrative Results

While the equations developed earlier are quite general, they also exhibit a very broad range of behaviors, and the formulation has 2 independent linear and 24 independent nonlinear coefficients. Notice that in reality, some of these parameters may be interconnected to each other, preventing us from isolating them separately in experiments. The model problems considered in this section allow us to isolate each parameter, and thus, help us understand their individual effects. This section works from simple cases that are amenable to analytical results and insights to a more involved problem that captures the observed dynamics. In particular, we start by analytically considering problems with frequency spacing, Δ, and one of the non-uniform parameters, $S_{2,10}$, set to zero in Section 4.2. Next, we consider the effects of $\Delta, S_{2,10}$, and noise in Section 4.3, showing how these introduce quasi-periodic oscillations as well as the system's preference in CW/CCW direction. Finally, we consider parametric noise, ξ_2, in Section 4.4, and show how it is needed to capture the simultaneous presence of standing and spinning wave attractors. We will consider the first azimuthal mode ($n = 1$) since that was the mode appeared in the experiments.

4.1 Model equations

In order to reduce the number of independent parameters, we consider the model equations in Eq. (17) below. First, without loss of generality, we define the azimuthal origin such that $S_{2,01} = 0$ [27]. Second, we consider a subset of the larger independent parameter space by (1) setting $C_{4,ij} = S_{4,ij} = 0$; this is equivalent to assuming that $4n$ non-uniformity is negligible relative to $2n$, and (2) setting the nonlinear coefficients, b_{30}, b_{12}, and b_{03} to zero. In the zero frequency spacing case that is analytically considered in the next section, these assumptions eliminate the coupling between amplitude and phase dynamics, enabling us to solve for all FP's and their stability. It will be shown later that the simulation with these assumptions still can capture the experimental observations quite well. The governing equations then simplify to:

$$\begin{aligned}
\dot{A} &= \frac{1}{4}\left[\beta\left(2 + C_{2,01}\right) - 2\alpha\right]A - k_{A1}S_{2,10}\sin\varphi\, B + k_{A2}A^3 + (k_3 - k_{A3}\cos 2\varphi)AB^2 + \frac{\Gamma}{4\bar{\omega}^3 A} + \frac{\zeta_A}{\bar{\omega}} \\
\dot{B} &= \frac{1}{4}\left[\beta\left(2 - C_{2,01}\right) - 2\alpha\right]B - k_{B1}S_{2,10}\sin\varphi\, A + k_{B2}B^3 + (k_3 - k_{B3}\cos 2\varphi)BA^2 + \frac{\Gamma}{4\bar{\omega}^3 B} + \frac{\zeta_B}{\bar{\omega}} \\
\dot{\varphi} &= \Delta - S_{2,10}\left(k_{B1}\frac{A}{B} - k_{A1}\frac{B}{A}\right)\cos\varphi + (k_{B3}A^2 + k_{A3}B^2)\sin 2\varphi + \left(\frac{1}{A} + \frac{1}{B}\right)\frac{\zeta_\varphi}{\bar{\omega}}
\end{aligned} \tag{17}$$

where

$$k_{A1} = \frac{b_{10}}{2(\Delta - 2)}, k_{B1} = \frac{b_{10}}{2(\Delta + 2)}, k_{A2} = \frac{b_{21}}{32}\left(3 + 2C_{2,21}\right), k_{B2} = \frac{b_{21}}{32}\left(3 - 2C_{2,21}\right) \tag{18}$$

$$k_3 = \frac{b_{21}}{16}, k_{A3} = \frac{b_{21}}{64}\left(\frac{3\Delta+2}{\Delta-2}\right), k_{B3} = \frac{b_{21}}{64}\left(\frac{3\Delta-2}{\Delta+2}\right)$$

The tildes on α, β and b_{ij} have been omitted. Recall that $C_{2,01}, S_{2,10}$ and $C_{2,21}$ are parameters that describe the non-uniformities in the source term response, such as dQ/dt, to $\dot{p}, p$, and $p^2\dot{p}$, respectively. Equation (17) will be used to simulate the dynamics of A, B, and φ, which will be mapped into F, G, and φ_{FG} using the following relationship:

$$\begin{aligned} F^2 &= \frac{1}{16}(A^2 + B^2 - 2AB\sin\varphi) \\ G^2 &= \frac{1}{16}(A^2 + B^2 + 2AB\sin\varphi) \\ \varphi_{FG} &= \arctan\left(\frac{2AB\cos\varphi}{A^2 - B^2}\right) \end{aligned} \tag{19}$$

The detailed derivation of Eq. (19) can be found in Appendix G.

4.2 Fixed points and their stability with $\Delta = S_{2,10} = 0$

This section considers the deterministic limit cycle solutions (i.e., the FPs of A, B, and φ) and their stability with the absence of pressure coupled azimuthal non-uniformity, $S_{2,10} = 0$, and no frequency shift, $\Delta = 0$. The effects of nonzero values of these parameters will be numerically investigated in Section 4.3. For the deterministic FP analysis, the time derivative of each variable and the noise terms are set to zero, leading to the following equations.

$$\begin{aligned} 0 &= \frac{1}{4}\left[\beta\left(2 + C_{2,01}\right) - 2\alpha\right]A + k_{A2}A^3 + (k_3 - k_{A3}\cos 2\varphi)AB^2 \\ 0 &= \frac{1}{4}\left[\beta\left(2 - C_{2,01}\right) - 2\alpha\right]B + k_{B2}B^3 + (k_3 - k_{B3}\cos 2\varphi)BA^2 \\ 0 &= (k_{B3}A^2 + k_{A3}B^2)\sin 2\varphi \end{aligned} \tag{20}$$

The FPs are given by:

$$\begin{aligned} &\text{FP\#1:} \quad A^{*2} = B^{*2} = 0 \\ &\text{FP\#2:} \quad A^{*2} = \frac{16\alpha - (16 + 8C_{2,01})\beta}{b_{21}(3 + 2C_{2,21})}, \quad B^{*2} = 0 \\ &\text{FP\#3:} \quad B^{*2} = \frac{16\alpha - (16 - 8C_{2,01})\beta}{b_{21}(3 - 2C_{2,21})}, \quad A^{*2} = 0 \\ &\text{FP\#4:} \quad A^{*2} = \frac{8\alpha\left(1 - C_{2,21}\right) - 4\beta\left(C_{2,01}\left(2 - C_{2,21}\right) + 2\left(1 - C_{2,21}\right)\right)}{b_{21}\left(2 - C_{2,21}^2\right)} \\ &\qquad\quad B^{*2} = \frac{8\alpha\left(1 + C_{2,21}\right) + 4\beta\left(C_{2,01}\left(2 + C_{2,21}\right) - 2\left(1 + C_{2,21}\right)\right)}{b_{21}\left(2 - C_{2,21}^2\right)} \\ &\qquad\quad \varphi^* = \pm\frac{\pi}{2}, \pm\frac{3\pi}{2}, \ldots \end{aligned} \tag{21}$$

where * is the value at each FP. Note that there are 4 possible solutions to this equation. Here, FP#1 is a zero amplitude, FPs #2 and #3 are purely standing waves orthogonal to each other (horizontal and vertical, respectively), and FP#4 is a mixed wave. When $C_{2,01} = C_{2,21} = 0$, FP#4 becomes a purely spinning wave whose direction is determined by its initial condition.

The physical realization of the above FPs depends on the stability of each FP, which can be assessed by using the Routh-Hurwitz (RH) criterion [60-63]. The RH criterion for each FP yields the following conditions.

$$\begin{aligned} &\text{FP\#1}: \gamma \le \gamma_{Hopf,1} \\ &\text{FP\#2, 3}: \gamma_{Hopf,1} < \gamma \le \gamma_{Hopf,2} \\ &\text{FP\#4}: \gamma > \gamma_{Hopf,2} \end{aligned} \tag{22}$$

where

$$\gamma = \beta/\alpha$$

$$\gamma_{Hopf,1} = \begin{cases} \dfrac{2}{2 + C_{2,01}}, & \text{if } 0 \le C_{2,01} < 1 \text{ (FP\#2)} \\ \dfrac{2}{2 - C_{2,01}}, & \text{if } -1 < C_{2,01} < 0 \text{ (FP\#3)} \end{cases} \tag{23}$$

$$\gamma_{Hopf,2} = \begin{cases} \dfrac{2(1 + C_{2,21})}{2(1 - C_{2,01}) + C_{2,21}(2 - C_{2,01})}, \text{if } 0 \le C_{2,01} < 1 \text{ and } C_{2,01} < \dfrac{2(C_{2,21} + 1)}{2 + C_{2,21}} & \text{(FP\#2)} \\ \dfrac{2(1 - C_{2,21})}{2(1 + C_{2,01}) - C_{2,21}(2 + C_{2,01})}, \text{if } -1 \le C_{2,01} < 0 \text{ and } C_{2,01} < \dfrac{2(C_{2,21} - 1)}{2 - C_{2,21}} & \text{(FP\#3)} \end{cases}$$

It has been assumed that the non-uniformity parameters, $C_{2,01}$ and $C_{2,21}$, are bounded between ± 1. This physically implies that the non-uniform parameters are less than the mean value in Eq. (11). Here, $\gamma_{Hopf,1}$ corresponds to the bifurcation from FP#1 (zero amplitude) to FP#2 or #3 (standing wave), and $\gamma_{Hopf,2}$ is the bifurcation from FP#2 or #3 (standing wave) to FP#4 (mixed wave). Figure 8 summarizes the stability of each FP in $(C_{2,01}, \gamma)$ space with different $C_{2,21}$ values. Here, the horizontal dash line indicates $\gamma = 1$, and the contour lines denote $|SR|$. Consider a case where γ is increasing with fixed values of $C_{2,01}$ and $C_{2,21}$. This is equivalent to moving in a vertical direction in the plot. As γ increases, a system transitions from FP#1 (zero amplitude) to FP#2 or #3 (standing wave), and then FP#4 (mixed wave). However, when $C_{2,01}$ is zero, the system transitions directly from FP#1 to FP#4. Specifically, when the system is azimuthally uniform, $C_{2,01} = C_{2,21} = 0$, the mode exists either as a zero amplitude or a purely spinning wave, depending upon γ. Also note from $\gamma_{Hopf,1}$ that the more $C_{2,01}$ deviates from zero, the lower γ the system becomes unstable at, i.e., the non-uniformity promotes linear instability. When being unstable, the system transitions towards the standing wave with $C_{2,01}$ deviating from zero. In this sense, $C_{2,01}$ resembles the resistive asymmetry, a_2, in [44]. Lastly, nonzero $C_{2,21}$ causes $\gamma_{Hopf,2}$ to be asymmetric about $C_{2,01} = 0$ line.

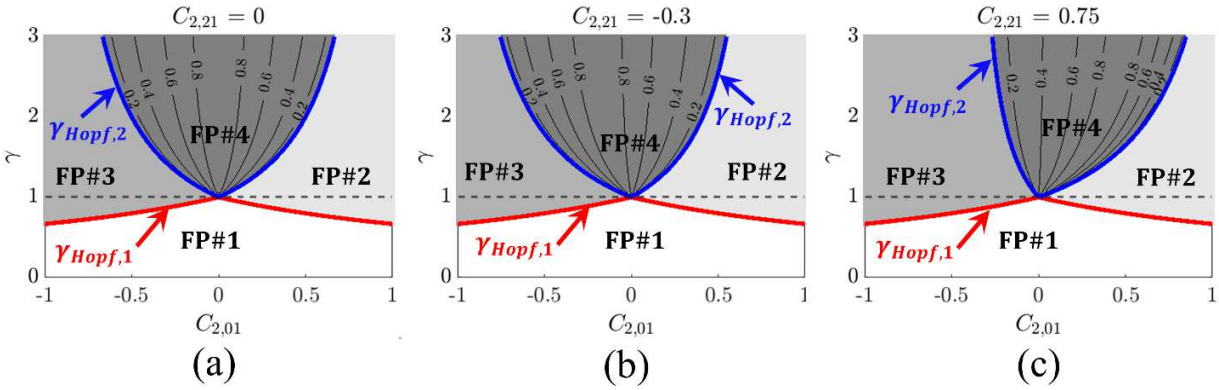

Fig. 8. Stability map in $(C_{2,01}, \gamma)$ space with difference $C_{2,21}$ values. Red and blue lines denote the first and second bifurcation boundaries. The horizontal dash line denotes $\gamma = 1$. Contour lines indicate $|SR|$.

To summarize, this figure clearly shows that under unstable conditions, the system can be dominated by standing, spinning, or mixed waves, and shows how the relative dominance of these waves is controlled by linear damping/growth rates, $(\gamma = \beta/\alpha)$, and azimuthal non-uniformities, $(C_{2,01}, C_{2,21})$.

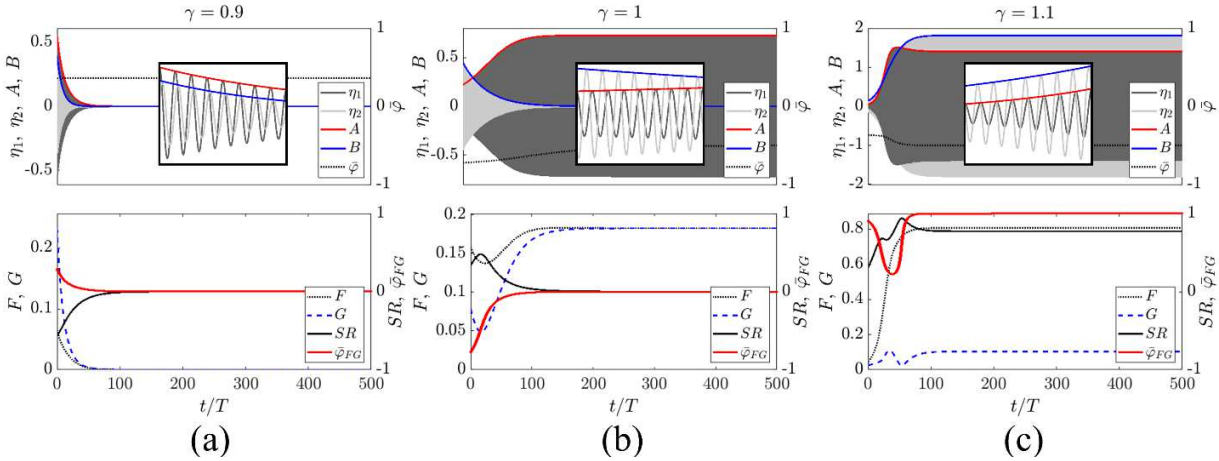

Fig. 9. Top: simulations of η_1, η_2, A, B, and $\bar{\varphi}$. Zoomed box describes the dynamics of the first eight cycles. Bottom: simulations of F, G, SR and $\bar{\varphi}_{FG}$. γ values are (a) 0.9, (b) 1, and (c) 1.1. The other parameters are $b_{21} = -0.05, C_{2,01} = 0.05, S_{2,10} = 0, C_{2,21} = 0.75, \bar{\omega} = 1, \Delta = 0, \Gamma = 0$. The Hopf bifurcation points calculated from Eq. (23) are $\gamma_{Hopf,1} = 0.9757, \gamma_{Hopf,2} = 1.041$.

Further insight into these FP's and their stability can be obtained from transient computations, showing the system's relaxation to these FP's from arbitrary initial conditions, see Fig. 9. The first row illustrates simulations of η_1, η_2, A, B, and $\bar{\varphi}$ with different γ values. Here, $\bar{\varphi} \equiv \varphi/\pi$. η_1 and η_2 are numerically obtained from Eq. (12), and A, B, and φ are from Eq. (17). Zoomed box in each plot demonstrates that the method of averaging technique closely captures the magnitudes of the second order oscillators. After each simulation, A, B, and φ are mapped into F, G, and φ_{FG} using Eq. (19). Lastly, SR is calculated by Eq. (3).

Figure 9(a) represents the zero amplitude mode (FP#1) where $\gamma < \gamma_{Hopf,1}$, and thus, both amplitudes, A and B, decay to zero, i.e., the system is linearly stable. In this case, $\bar{\varphi}, SR$, and $\bar{\varphi}_{FG}$ do not have any physical meaning.

Figure 9(b) is the case where $\gamma_{Hopf,1} < \gamma < \gamma_{Hopf,2}$, and the system is linearly unstable. As expected from Eq. (23), FP#2 is stable, and only A converges to a finite value because $C_{2,01} > 0$. The bottom plot shows that F and G converge to the same value, resulting in zero SR or a purely standing wave. Also note that $\bar{\varphi}_{FG}$ converges to zero, implying from Eq. (5) that the anti-nodal line ($\theta_a = -\varphi_{FG}/2$) is located horizontally. This is physically reasonable because the flames that strongly couple with acoustics are oriented in the horizontal direction for positive $C_{2,01}$.

Further increase in $\gamma > \gamma_{Hopf,2}$ leads to a mixed wave as shown in Fig. 9(c) where both A and B converge to finite values. This state corresponds to FP#4 in Eq. (21). In the bottom plot, F is greater than G at a steady state, and thus, $SR > 0$. Notice that $\bar{\varphi}_{FG}$ converges to 1, indicating that the anti-nodal line of the mixed wave is in a vertical direction.

Finally, note that, near the FP values, both A and B relax towards their equilibrium values as damped exponentials for all cases; i.e., they do not exhibit decaying oscillations as they asymptote to their FPs. As discussed in the next section, this is not true in general and, even in cases where the FPs are stable, damped oscillations about the FPs are possible. In this case, these systems exhibit significantly different behavior in the presence of background noise.

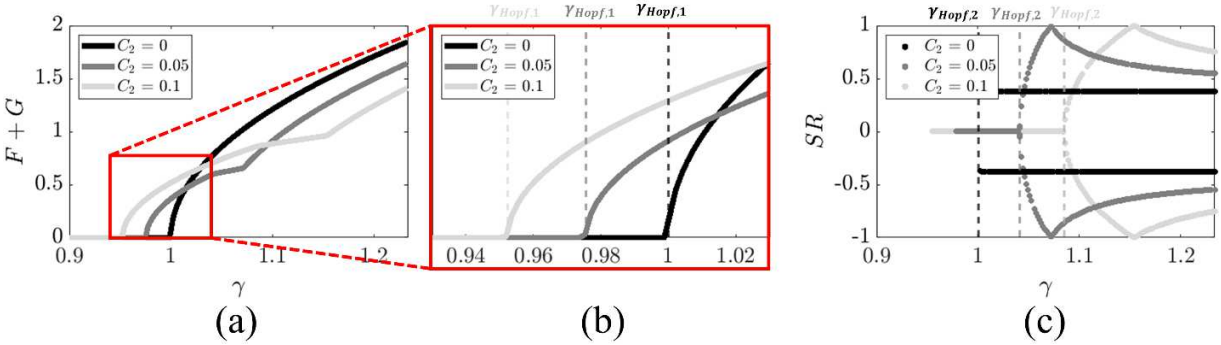

Fig. 10. (a) Pressure anti-node magnitude as a function of γ with different $C_{2,01}$ values. (b) Zoomed in frame of (a). (c) SR as a function of γ with different $C_{2,01}$ values. The other parameters are $b_{21} = -0.05, S_{2,10} = 0, C_{2,21} = 0.75, \bar{\omega} = 1, \Delta = 0, \Gamma = 0$. The grayscale vertical lines in (b) and (c) denote the first and second bifurcation points, respectively.

Figure 10(a) describes the effect of linear damping/growth rate, γ, on the steady state pressure anti-node magnitude with different $C_{2,01}$ values, obtained from computational solutions. Here, the simulation was run out to sufficient time to reach a steady state, and was repeated at different initial conditions to explore their effects. For reference, Fig. 10(b) shows a detail of Fig. 10(a) with the dashed vertical lines indicating the theoretical predictions for the bifurcation points, $\gamma_{Hopf,1}$. Note the excellent agreement between these computed results and Eq. (23). As expected from Eq. (23), the first Hopf bifurcation point, $\gamma_{Hopf,1}$, decreases with increasing $C_{2,01}$. In other words, the larger the azimuthal non-uniformity, the earlier the system becomes unstable. The figure also shows that the higher the non-uniformity, the slower the instability amplitude grows with γ.

Figure 10(c) plots SR as a function of γ with different $C_{2,01}$ values, showing the presence

of purely standing and spinning waves, as well as mixed waves. When $C_{2,01} = 0$, the azimuthal mode has a constant $SR = \pm 0.38$, or a mixed wave. For $C_{2,01} > 0$, SR starts from zero at $\gamma = \gamma_{Hopf,1}$ and maintains this value until $\gamma = \gamma_{Hopf,2}$. After $\gamma_{Hopf,2}$, SR first rapidly approaches a purely spinning wave value of ± 1 and then decays to a mixed wave. Comparing different $C_{2,01}$ cases, $\gamma_{Hopf,2}$ increases with increasing $C_{2,01}$, i.e., the non-uniformity delays the transition from a standing to a mixed wave. Note that there are two branches, positive and negative SR. Which branches the system is stabilized at depends on the initial conditions. These simulated results are consistent with the analytical results plotted in Fig. 8(c).

Figure 10(c) demonstrates that the system does not exhibit a standing wave limit cycle when $C_{2,01} = 0$. However, the experimental data in Fig. 4(a) shows the standing wave even in the nominally "uniform" fuel staging case, implying that the value of $C_{2,10}$ in our facility is actually nonzero. This is probably due to inevitable manufacturing differences, leakage flows, and so forth. As such, these results show that relatively small manufacturing variations can introduce significant impacts on the dominance of spinning/standing waves, and so forth (e.g., see Fig. 8), and also suggest that these behaviors can vary between engines.

4.3 Frequency shift and pressure coupled azimuthal non-uniformity effects

Having considered the basic FPs and their stability, this section considers the important generalization of more general azimuthal non-uniformities (i.e., nonzero $S_{2,10}$) and frequency spacing between the two eigenmodes. Although analytical solutions are not possible for these cases, some insights into their behavior (which are confirmed from the computations shown later) can be obtained from consideration of the equation structure for small perturbations about the FPs derived in the prior section, denoted by A^* and B^*. The equation for φ can be written in a "potential form" as:

$$\dot{\varphi} = -\frac{dU}{d\varphi} \tag{24}$$

where the "potential" U is given by:

$$U = -\varphi\Delta + S_{2,10}\left(k_{B1}\frac{A^*}{B^*} - k_{A1}\frac{B^*}{A^*}\right)\sin\varphi + \frac{1}{2}\left(k_{B3}A^{*2} + k_{A3}B^{*2}\right)\cos 2\varphi \tag{25}$$

and, consistent with the approximation of considering very small departures of the system from the Section 4.2 analysis, it has been assumed that the amplitudes, A and B, are constant at their FP values, A^* and B^* in this equation [34]. The potential in Eq. (25) consists of three terms: the first term, proportional to Δ, causes φ to drift in one direction linearly with time. The second term, proportional to $S_{2,10}$, provides one-well potential at either CW or CCW spinning wave, which is determined by the sign of the second term. The third term, proportional to k_{A3} and k_{B3}, provides two-well potential at both CW/CWW spinning waves. Figure 11 shows each term as a function of φ and their contribution to the potential shape for two different cases. The figure clearly shows that $S_{2,10}$ term causes a preference to either CW or CCW spinning wave. When this term is sufficiently larger than the other terms, it will suppress one of the spinning waves, and foster the

other (Fig. 11(a)). In this aspect, the nonzero $S_{2,10}$ is similar to the situation in [44] where the angles of resistive and reactive asymmetry are not aligned, i.e., $\Theta_{\mu 2} \neq \Theta_{\alpha 2}$. In contrast, when Δ term dominates over the other terms, φ can continuously drift in one direction (Fig. 11(b)) without a local minimum, which serves as a local attractor. As can be seen in Eq. (19), this drift causes not only the out-of-phase oscillations between CW/CCW amplitudes, resulting in the oscillation of SR, but also the oscillation in φ_{FG}, both of which were observed experimentally as the quasi-periodic standing wave. Recall that the frequency difference, Δ, is controlled by the non-uniform parameter, $C_{2,10}$, in Eq. (13). This means that the quasi-periodicity shows up only if $C_{2,10}$ is nonzero. In this sense, the term, $C_{2,10}$, resembles the reactive asymmetry, m_2, in [44].

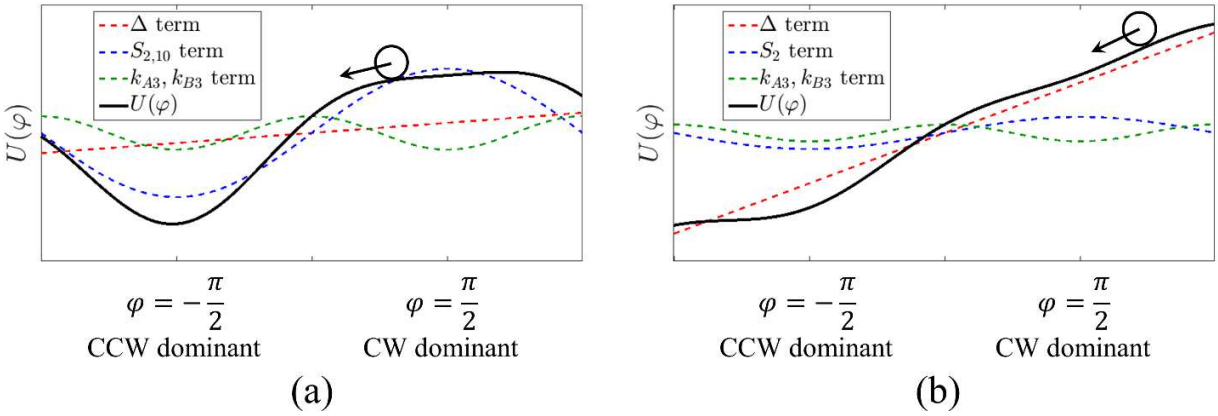

Fig. 11. "Potential" and contributions of each term to its shape for two example cases (a) $S_{2,10}$ term dominant system, leading to a local minimum in U, (b) Δ term dominant system, which has no local minimum in U.

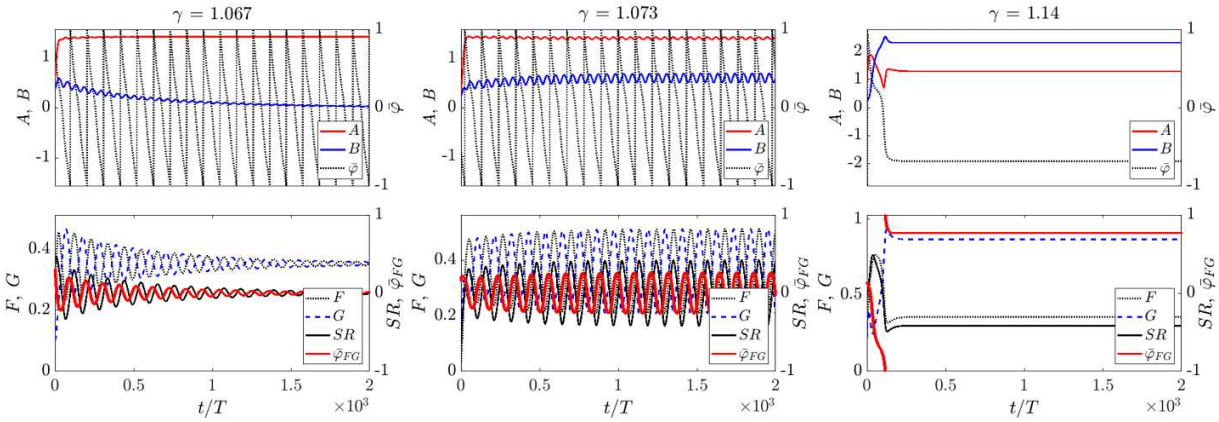

Fig. 12. Top: simulations of A, B, and $\bar{\varphi}$. Bottom: simulations of F, G, SR and $\bar{\varphi}_{FG}$. γ values are (a) 1.067, (b) 1.073, and (c) 1.14. The other parameters are $b_{21} = -0.05, C_{2,01} = 0.05, S_{2,10} = 0, C_{2,21} = 0.75, \bar{\omega} = 1, \Delta = -0.01, \Gamma = 0$.

We next present computations, starting first with the case where $S_{2,10} = 0$, but $\Delta \ll 1$. Notice that in the linear regime, a nonzero Δ imposes two different frequencies on the system. Depending upon the value of Δ, the ratio of the two frequencies may be irrational (i.e., quasi-

periodic) or rational (leading to period-N oscillations, with the value of N being a function of Δ). Even if it is rational, if $\Delta \ll 1$, then N becomes so large that the system appears as quasi-periodic in real applications. Thus, we will use the word 'quasi-periodic' in the rest of this paper.

While a nonzero Δ implies a system with two distinct frequencies in the linear case, it does not necessarily do so in the nonlinear case at steady state conditions. Nonlinearities do this in two ways – first, through amplitude dependent frequency shifts which can synchronize the two distinct frequencies and, second, by "quenching", where two linearly unstable oscillators compete with each other and one oscillator's amplitude is driven to zero. Both behaviors are illustrated in Fig. 12. The first row of Fig. 12(a) shows the simulations of $A, B,$ and $\bar{\varphi}$ with a finite frequency spacing, showing how the system relaxes to "steady state" from a prescribed initial condition. In contrast to Fig. 9(a), note from the second row of Fig. 12(a) how F and G decay in an oscillatory manner towards the FP at the frequency of Δ, evidence of a damped quasi-periodic solution. However, the quasi-periodicity disappears at a steady state because one of the oscillators (B in this case) decays to zero, resulting in a single frequency oscillation. In other words, nonlinear competition between the two standing eigenmodes leads to quenching of oscillator B, even though both oscillators are linearly unstable.

An increase in γ causes a self-sustained quasi-periodic oscillation as shown in Fig. 12(b). Note from the first row that the two oscillators coexist, and their phase difference drifts in one direction, demonstrating the presence of two different frequencies in the system. The second row in Fig. 12(b) shows that both SR and $\bar{\varphi}_{FG}$ oscillate around zero, and the phase lag between them is about 90°. This is in good agreement with the quasi-periodic standing wave observed in the experiments, e.g., Fig. 4(a).

Further increase in γ alters the system to a mixed wave as shown in Fig. 12(c). The first row shows that the two oscillators coexist, but their phase difference is constant at a steady state, indicating that their oscillation frequencies are synchronized. Thus, the quasi-periodicity vanishes as shown in the second row of Fig. 12(c).

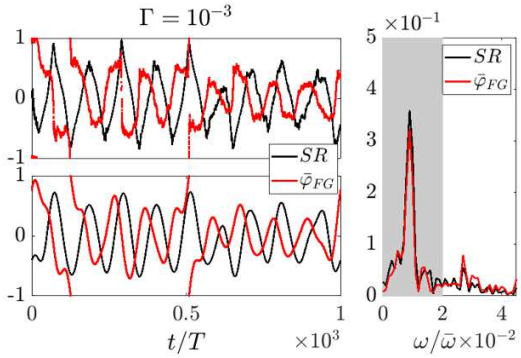

Fig. 13. Simulation of SR and $\bar{\varphi}_{FG}$ with background noise intensity, $\Gamma = 10^{-3}$. Top left: raw signal. Bottom left: filtered signal. Right: Fourier transform. The shaded region in the Fourier transform denotes the low pass filter width. The other parameters are $\gamma = 1.067, b_{21} = -0.05, C_{2,01} = 0.05, S_{2,10} = 0, C_{2,21} = 0.75, \bar{\omega} = 1, \Delta = -0.01$.

Figure 12(a) shows that quasi-periodic behavior only appears during the initial transient, as the oscillator B is damped. However, in the presence of background noise, the damped oscillator B will be continuously excited and the phase averaged system will be quasi-periodic. To illustrate, Fig. 13 plots representative time traces and corresponding spectra of SR and $\bar{\varphi}_{FG}$ for the same

parameter set with Fig. 12(a), but with background noise. The white noise terms in Eq. (17) have been simulated using the Euler-Maruyama scheme [64]. Notice that introducing the background noise prevents the SR and $\bar{\varphi}_{FG}$ from decaying to zero, causing them to continuously oscillate around zero, i.e., as a quasi-periodic standing wave. In addition, Fig. 13 shows that sufficiently high noise intensity may cause $\bar{\varphi}_{FG}$ to jump from ± 1 to ∓ 1, e.g., at $t/T = 500$, which was seen experimentally in other studies [40]. Recalling that $\bar{\varphi}_{FG}$ is directly related to the anti-nodal line by Eq. (5), this demonstrates the rotation of the anti-nodal line in the CW/CCW direction.

To summarize, even very small frequency shifts have profound influences on system dynamics. This is shown in the first three rows of Fig. 14(a), which generalizes Fig. 10(c), plotting SR as a function of γ at different $C_{2,01}$ values for a noise free system, $\Gamma = 0$. $\gamma_{Hopf,2}$ for $\Delta = 0$ is indicated for comparison. Note that nonzero Δ shifts the second bifurcation points from the $\gamma_{Hopf,2}$ values analytically calculated in Eq. (23). The largest qualitative change is the quasi-periodic regimes. The system with nonzero Δ and $C_{2,01}$ exhibits quasi-periodic behavior for a certain range of γ without the noise contribution. However, the last row of Fig. 14(a) shows that when exposed to the noise, the quasi-periodic behavior appears from the onset of instability to right before the mixed wave solutions. This makes it difficult to differentiate between noise-driven and self-sustained quasi-periodic behavior from the time trace data (Fig. 13) or the bifurcation plot (the last row of Fig. 14(a)). They can be differentiated, however, from the average phase portrait, such as shown in Fig. 14(b). The phase portrait was obtained by repeating the simulations at distributed initial conditions over the phase space. The top and the bottom of Fig. 14(b) are the phase portraits with the same condition as Fig. 13 and Fig. 12(b), respectively, with noise contribution. It can be seen that the center point is an attractor for the noise-driven quasi-periodic case, whereas it is a repeller for the self-sustained quasi-periodic case. Also note that for the self-sustained case, the trajectory and the joint PDF form a ring structure around the center. Considering the experimental data, this suggests that the FP in Fig. 5(a) corresponds to a noise-driven quasi-periodic standing wave, and the center FP in Fig. 18(b) is a self-sustained quasi-periodic standing wave.

It is also interesting to note that the trajectories are CW spiraling into/around the FP in Fig. 14(b). As mentioned before, this is due to the 90° phase lag between SR and $\bar{\varphi}_{FG}$ oscillations. If SR and $\bar{\varphi}_{FG}$ exponentially decay to their FPs without oscillations such as a mixed wave solution in Fig. 12(c), the trajectories in the phase portrait would directly converge to the FP without the spiraling. This behavior was observed experimentally in Fig. 5(c).

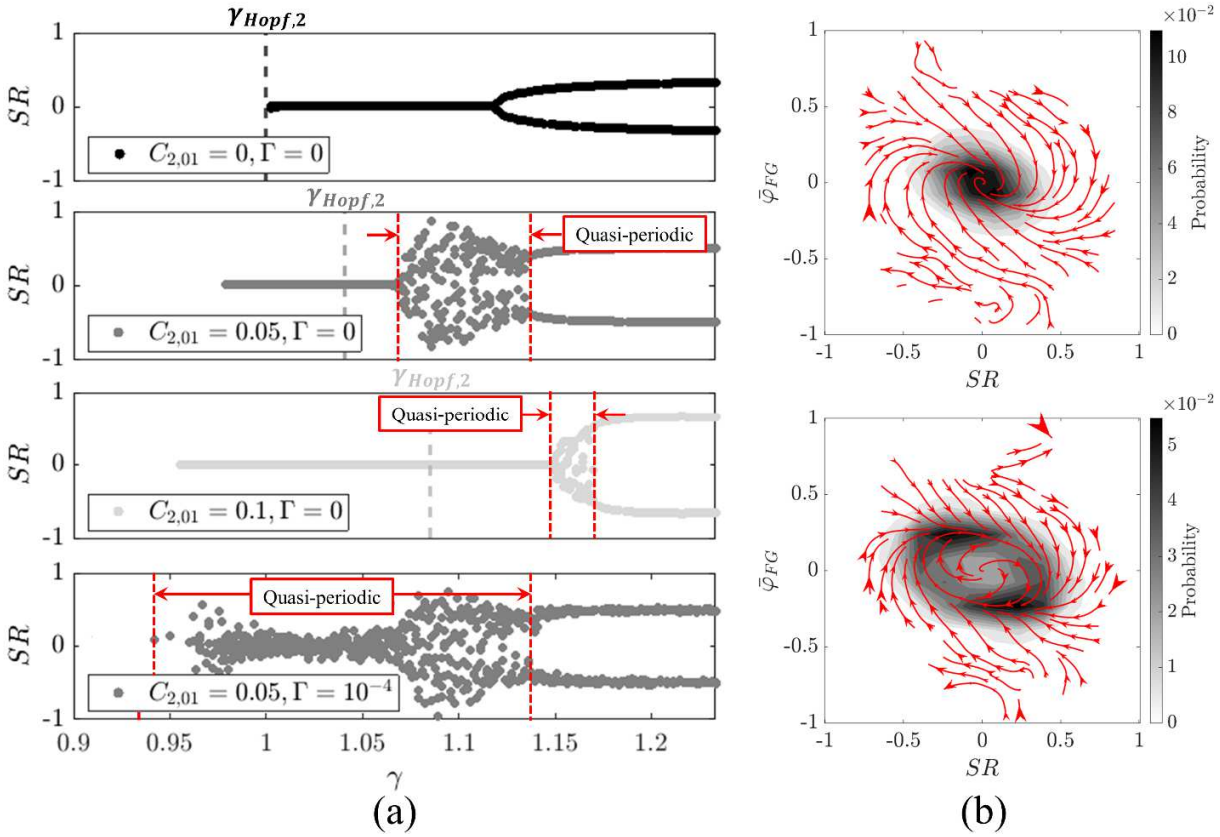

Fig. 14. (a) 1st – 3rd rows: SR as a function of γ with different $C_{2,01}$ values without noise. The grayscale vertical lines denote the second bifurcation point, $\gamma_{Hopf,2}$, when $\Delta = 0$. 4th row: SR as a function of γ with noise. The data points with an anti-node magnitude less than 0.1 are omitted because of their large fluctuations. The red vertical lines denote the quasi-periodic standing wave regions. The other parameters are $b_{21} = -0.05, S_{2,10} = 0, C_{2,21} = 0.75, \bar{\omega} = 1, \Delta = -0.01$. (b) Average phase portrait in SR and $\bar{\varphi}_{FG}$ space. Top: $\gamma = 1.067$, bottom: $\gamma = 1.073$. The other parameters are $b_{21} = -0.05, C_{2,10} = 0.05, S_{2,10} = 0, C_{2,21} = 0.75, \bar{\omega} = 1, \Delta = -0.01, \Gamma = 10^{-4}$.

We close this subsection by introducing a bifurcation plot in $(C_{2,01}, \gamma)$ space for the noise free system, which is similar to Fig. 8, but with a finite frequency spacing. Figure 15 shows regions where the system exhibits zero amplitude (linearly stable), single frequency standing waves (i.e., nonlinear effects lead to quenching of one of the standing eigenmodes), self-sustained quasi-periodic standing waves, and single frequency mixed waves (i.e., not purely standing or spinning). This plot shows a region where the quasi-periodic behavior can occur with a noise free system. The region becomes wider with increasing frequency split. Note that even if the system's parameters are not inside the region, but close to it, the system exhibits damped oscillation during the initial transient as shown in Fig. 12(a). However, when the system moves far away from the region, the oscillatory behavior disappears even with the noise contribution.

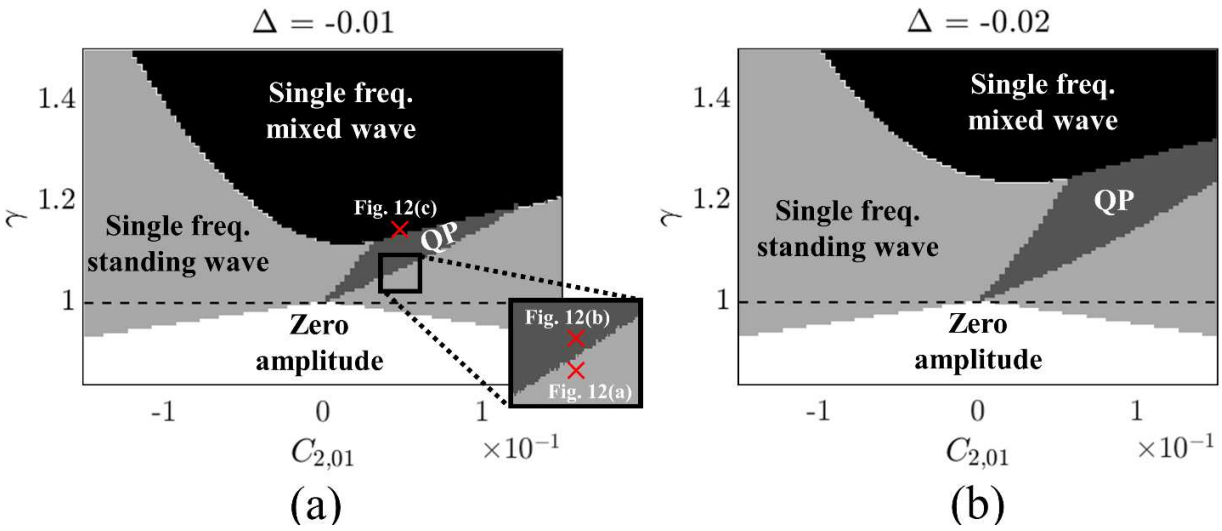

Fig. 15. Bifurcation plot in $(C_{2,01}, \gamma)$ space showing quasi-periodic behavior with two different frequency spacing values (a) $\Delta = -0.01$ and (b) $\Delta = -0.02$. Here, QP = quasi-periodic standing wave region. The horizontal dash line denotes $\gamma = 1$. The red crosses in (a) indicate $(C_{2,01}, \gamma)$ in Fig. 12(a)-(c). The other parameters are $b_{21} = -0.05, S_{2,10} = 0, C_{2,21} = 0.75, \bar{\omega} = 1, \Gamma = 0$.

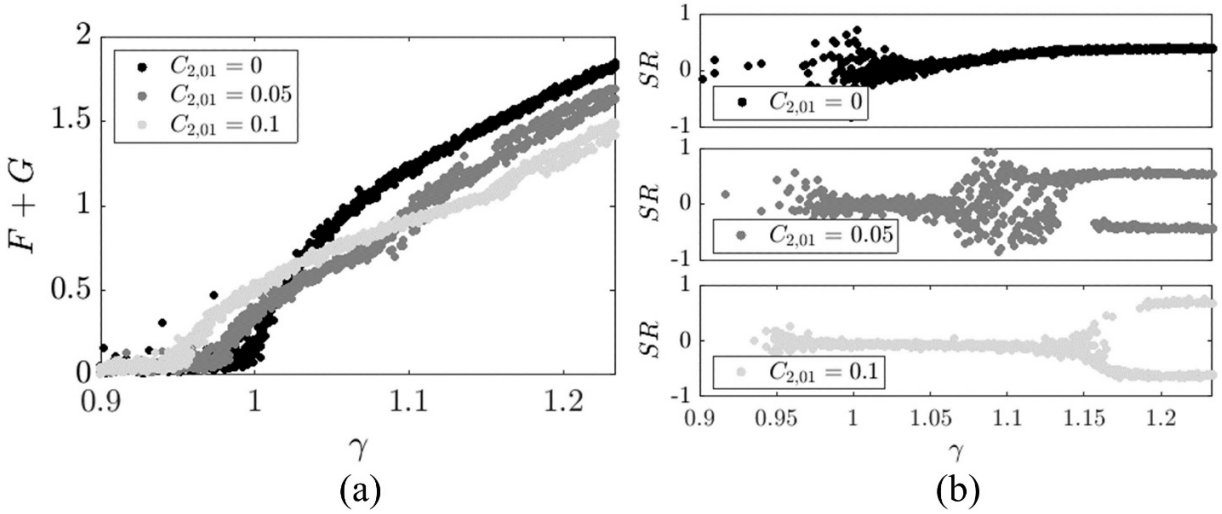

Fig. 16. (a) Pressure anti-node magnitude as a function of γ with different $C_{2,01}$ values. (b) SR as a function of γ with different $C_{2,01}$ values. The data points with an anti-node magnitude less than 0.1 are omitted because of their large fluctuations. The other parameters are $b_{21} = -0.05, S_{2,10} = 0.02, C_{2,21} = 0.75, \bar{\omega} = 1, \Delta = -0.01, \Gamma = 10^{-4}$.

We conclude this section by considering the general case where the pressure coupled non-uniformity, $S_{2,10}$, frequency spacing, Δ, and noise, Γ, are all present. Figure 16(a) plots computated results for the anti-node pressure magnitude as a function of γ and $C_{2,01}$. Although the system is linearly stable, the magnitudes are nonzero because of the noise contribution. Other than that, Fig. 16(a) exhibits similarities to those in Fig. 10(a). For example, the first bifurcation point is delayed as $C_{2,01}$ gets close to zero, but its amplitude grows faster with γ. Notice that Fig. 16(a) also

resembles the experimental results from $OR = 0.5$ to 0.55 in Fig. 6(a).

Figure 16(b) represents a similar plot with the last row of Fig. 14(a), but with a finite non-uniformity, $S_{2,10}$. The figure clearly shows that $S_{2,10}$ imposes a preferential spinning direction. For $C_{2,01} = 0$, a system has a preference in a positive SR or CCW direction. For $C_{2,01} = 0.05$, the system still prefers CCW to CW after the quasi-periodic standing wave, but CW direction also appears above $\gamma = 1.16$. In contrast, the system with $C_{2,01} = 0.1$ has a preference in the CW direction. The change in preferential direction is due to the sign change of the second term in Eq. (25). To summarize, introducing the non-uniformity, $S_{2,10}$, causes a mixed/spinning wave to be biased towards either CW or CCW direction. This provides a possible explanation for why the experimental data shown in Fig. 4(c) show a bias towards positive SR values.

4.4 Intermittency and parametric noise effects, ξ_2

This section considers parametric noise effects which, as noted in prior studies, introduce qualitatively new phenomena [65-68]. As noted in the prior sections, certain features of the data can be understood from purely deterministic considerations, some require additive noise, and, as discussed here, some also require introducing parametric noise. In particular, within the modeling assumptions described in section 4.1, parametric noise is required to capture the intermittency between the standing and mixed waves observed experimentally because these solutions are not simultaneously stable, as shown in Eq. (22). Specifically, given the fact that the behavior of SR abruptly changes with γ, or equivalently β, for $C_{2,01} > 0$ as illustrated in Fig. 16(b), parametric noise in β will lead to intermittency. To illustrate, we consider parametric fluctuations in the parameter β, i.e., $h_2(p, \dot{p}) = \beta\dot{p}$, and assume that the noise term, $\xi_2(t)$, follows the Ornstein–Uhlenbeck (OU) process [69], which drifts toward its mean value over time, numerically simulated with the Euler-Maruyama scheme [64]. This process is more appropriate than the Brownian motion, where the variance grows with time (i.e., in an unbounded fashion); in contrast, the variance for the OU process reaches a constant value.

Figure 17 illustrates three representative cases with $C_{2,01} = 0.05$ where the asymptotic means of $\gamma(t)$ are $\bar{\gamma} = 1.033, 1.117,$ and 1.2. Figure 17(a) - (c) describe the time trace of $\gamma(t)$ (top) as well as SR and $\bar{\varphi}_{FG}$ (middle), and the last row of Fig. 17 represents the average phase portrait for each case.

For $\bar{\gamma} = 1.033$ (Fig. 17(a)), both SR and $\bar{\varphi}_{FG}$ fluctuate around zero. Note that the modulation amplitude is not steady as opposed to Fig. 13 because of time varying $\gamma(t)$. The dynamics of SR and $\bar{\varphi}_{FG}$ resemble the experiments in Fig. 4(a) except that $\bar{\varphi}_{FG}$ oscillates around 0.4. Given the fact that $\bar{\varphi}_{FG}$ is related to the anti-nodal line (Eq. (5)), the value of which depends on the azimuthal origin, the discrepancy can be eliminated by rotating the origin. The phase portrait in Fig. 17(a) shows a stable attractor at the center (A_S), and the trajectories are CW spiraling into the attractor. These results resemble the experimental observations in Fig. 5(a).

When $\bar{\gamma} = 1.117$, SR and $\bar{\varphi}_{FG}$ start to show intermittency. In particular, the transition of SR and $\bar{\varphi}_{FG}$ from one state to the other occurs simultaneously, which was evident from the experiments in Fig. 4(b). In the simulation, they are hopping between three different states, i.e., quasi-periodic standing wave, and CCW/CW mixed waves. The phase portrait in Fig. 17(b) reveals three attractors, $A_S, A_{CW/CCW}$, as well as multiple saddle points. Notice that the joint PDF around A_{CCW} is denser than that around A_{CW}, manifesting the system's preference in a CCW mixed wave. The portrait reasonably coincides with Fig. 5(b).

Lastly, for $\bar{\gamma} = 1.2$ (Fig. 17(c)), SR stays either ± 0.5, and $\bar{\varphi}_{FG}$ remains around ± 1. The

transition between two states may occur when $\gamma(t)$ drops below a certain value. The corresponding phase portrait in Fig. 17(c) manifests two stable attractors, $A_{CW/CCW}$, and multiple saddle points. Here, A_S is no longer a stable attractor, which explains the reason for no realization at the center in Fig. 5(c). Similar to Fig. 17(b), the joint PDF demonstrates the preference in the CCW spinning wave. By comparing with Fig. 5(c), notice the similarities.

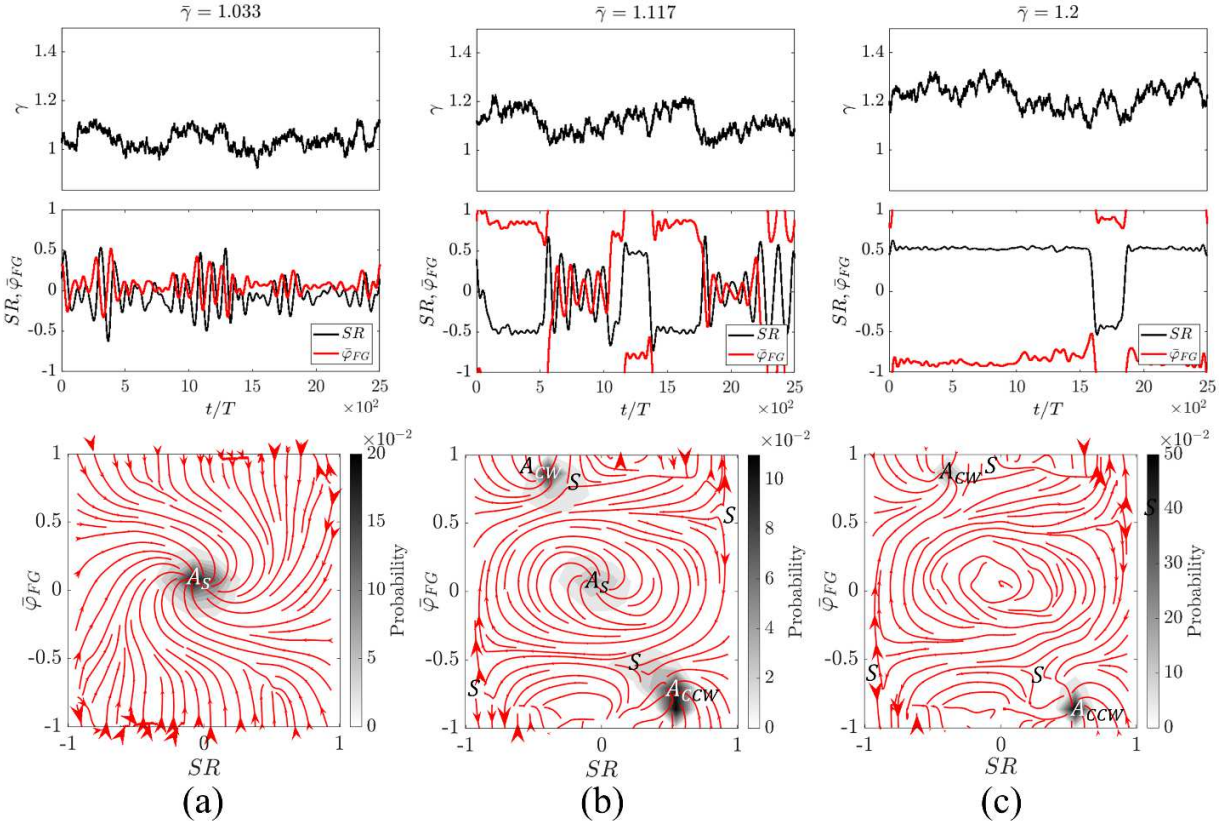

Fig. 17. Top: time series simulation of $\gamma(t)$ for (a) $\bar{\gamma} = 1.033$, (b) $\bar{\gamma} = 1.117$, (c) $\bar{\gamma} = 1.2$. Middle: dynamics of SR and $\bar{\varphi}_{FG}$ for each $\bar{\gamma}$. Bottom: simulated phase portrait for each $\bar{\gamma}$. The other parameters are $b_{21} = -0.05, C_{2,01} = 0.05, S_{2,10} = 0.02, C_{2,21} = 0.75, \bar{\omega} = 1, \Delta = -0.01, \Gamma = 10^{-4}$.

5. Conclusion

This paper presented experimental and modeling work to better understand wave structures and temporal dynamics of azimuthal modes in combustors. The experimental data was obtained from an industrial-scale combustor, specifically developed to control the azimuthal fuel distribution. For the uniform staging, the azimuthal mode exhibited a variety of behaviors, e.g., quasi-periodic standing, mixed waves as well as intermittency. When the fuel was staged in a non-uniform manner, however, only the quasi-periodic standing wave was observed.

In order to capture these dynamics, the paper developed a weakly nonlinear model, derived from the wave equation and a generalized source term. The source term was modeled with a Taylor expansion up to fourth order with the additive and parametric noise terms. Each coefficient in the expansion was allowed to vary azimuthally. This model clearly showed that these coefficients influence the azimuthal mode stability as follows.

- Linear damping/growth rates, α and β, determines the linear stability of two standing eigenmodes.
- The parameter, $C_{2n,01}$, describing the azimuthal non-uniform coupling between the source and $\dot{p}$, influences both linear (stability boundary) and nonlinear processes (dependence of limit cycle amplitude, such as upon β). It also affects relative preference between standing and spinning/mixed waves.
- The parameter, $C_{2n,21}$, describing the azimuthal non-uniform coupling between the source and $p^2\dot{p}$, affects relative preference between standing and spinning/mixed waves.
- The parameter, $S_{2n,10}$, describing the azimuthal non-uniform coupling between the source and p, introduces a preference in CW/CCW spinning direction on the system.
- The parameter, $C_{2n,10}$, describing the azimuthal non-uniform coupling between the source and p, causes a frequency spacing between the two orthogonal standing eigenmodes, Δ, which introduces quasi-periodic oscillations. The system can decay or self-excited in an oscillatory manner depending upon β.
- Additive noise, Γ, with nonzero Δ leads to quasi-periodic oscillations, even in cases where the limit cycle FP is stable, as it excites oscillatory, but decaying, disturbances around the limit cycle FP at a specific frequency, Δ.
- Parametric noise, $\xi_2(t)$, is responsible for the intermittency between standing and spinning/mixed waves.

The low order modeling was clearly useful in understanding the experimental observations. First, the instability magnitude increases with linear growth rate (or mass flow rates), but the rate of increase is reduced with increasing the non-uniformity (or OR). Second, as the magnitude increases, the azimuthal mode starts from a standing wave, passes the intermittency between standing and mixed waves, and then becomes a mixed wave. Third, a quasi-periodic oscillation appears during the standing wave. Last, the mode prefers CCW to CW spinning direction during the mixed wave. Finally, the model clearly emphasized that important real world effects, such as azimuthal asymmetry, introduce qualitatively important phenomena, such as quasi-periodicity.

Declaration of Competing Interest

The authors declare that they have no known competing financial interests or personal relationships that could have appeared to influence the work reported in this paper.

Acknowledgments

This work has been supported by the US Department of Energy through the University Turbine Systems Research program under contract DE-FE0031285 monitored by Mark Freeman.

References

[1] T.C. Lieuwen, Unsteady combustor physics, Cambridge University Press, Cambridge, U.K., 2012.
[2] T.C. Lieuwen, V. Yang, Combustion instabilities in gas turbine engines: operational experience, fundamental mechanisms, and modeling, American Institute of Aeronautics and Astronautics,

Reston, VA, 2005.
[3] H. Mongia, T. Held, G. Hsiao, R. Pandalai, Incorporation of combustion instability issues into design process: GE aeroderivative and aero engines experience, Progr Astronaut Aero, (2005) 43.
[4] K.O. Smith, J. Blust, Combustion instabilities in industrial gas turbines: Solar turbines' experience, Progr Astronaut Aero, (2005) 29-42.
[5] W. Krebs, S. Bethke, J. Lepers, P. Flohr, B. Prade, C. Johnson, S. Sattinger, Thermoacoustic design tools and passive control: Siemens power generation approaches, Progr Astronaut Aero, (2005) 89.
[6] M. Zellhuber, C. Meraner, R. Kulkarni, W. Polifke, B. Schuermans, Large eddy simulation of flame response to transverse acoustic excitation in a model reheat combustor, J Eng Gas Turb Power 135 (2013) 091508.
[7] J. O'Connor, V. Acharya, T. Lieuwen, Transverse combustion instabilities: Acoustic, fluid mechanic, and flame processes, Prog Energ Combust 49 (2015) 1-39.
[8] J.B. Sewell, P.A. Sobieski, Monitoring of combustion instabilities: Calpine's experience, Progr Astronaut Aero 210 (2005) 147-162.
[9] H. Ebrahimi, Overview of gas turbine augmentor design, operation, and combustion oscillation. 42nd AIAA/ASME/SAE/ASEE Joint Propulsion Conference & Exhibit (2006), 4916.
[10] D.E. Rogers, F.E. Marble, A mechanism for high-frequency oscillation in ramjet combustors and afterburners, J Jet Propulsion 26 (1956) 456-462.
[11] I. Elias, Acoustical Resonances Produced by Combustion of a Fuel-Air Mixture in a Rectangular Duct, J Acoust Soc Am 31 (1959) 296-304.
[12] W. Kaskan, A. Noreen, High-frequency oscillations of a flame held by a bluff body, Trans ASME 77 (1955) 855-891.
[13] N.A. Worth, J.R. Dawson, Effect of equivalence ratio on the modal dynamics of azimuthal combustion instabilities, P Combust Inst 36 (2017) 3743-3751.
[14] M. Mazur, H.T. Nygård, J.R. Dawson, N.A. Worth, Characteristics of self-excited spinning azimuthal modes in an annular combustor with turbulent premixed bluff-body flames, P Combust Inst 37 (2019) 5129-5136.
[15] K. Prieur, D. Durox, T. Schuller, S. Candel, Strong azimuthal combustion instabilities in a spray annular chamber with intermittent partial blow-off, J Eng Gas Turb Power 140 (2018) 031503.
[16] F.M. Berger, T. Hummel, M. Hertweck, J. Kaufmann, B. Schuermans, T. Sattelmayer, High-Frequency Thermoacoustic Modulation Mechanisms in Swirl-Stabilized Gas Turbine Combustors—Part I: Experimental Investigation of Local Flame Response, J Eng Gas Turb Power 139 (2017) 071501.
[17] J. Cohen, G. Hagen, A. Banaszuk, S. Becz, P. Mehta, Attenuation of gas turbine combustor pressure oscillations using symmetry breaking, 49th AIAA Aerospace Sciences Meeting, Orlando, FL, 2011.
[18] J.R. Dawson, N.A. Worth, Flame dynamics and unsteady heat release rate of self-excited azimuthal modes in an annular combustor, Combust Flame 161 (2014) 2565-2578.
[19] N.A. Worth, J.R. Dawson, Modal dynamics of self-excited azimuthal instabilities in an annular combustion chamber, Combust Flame 160 (2013) 2476-2489.
[20] P. Wolf, G. Staffelbach, L.Y. Gicquel, J.-D. Müller, T. Poinsot, Acoustic and large eddy simulation studies of azimuthal modes in annular combustion chambers, Combust Flame 159 (2012) 3398-3413.
[21] T. Poinsot, P. Wolf, G. Staffelbach, L. Gicquel, J. Muller, Identification of azimuthal modes

in annular combustion chambers, Center for Turbulence Research Annual Research Briefs, 2011.
[22] G. Staffelbach, L. Gicquel, G. Boudier, T. Poinsot, Large Eddy Simulation of self excited azimuthal modes in annular combustors, P Combust Inst 32 (2009) 2909-2916.
[23] C. Pankiewitz, T. Sattelmayer, Time domain simulation of combustion instabilities in annular combustors, J Eng Gas Turb Power 125 (2003) 677-685.
[24] D. Laera, T. Schuller, K. Prieur, D. Durox, S.M. Camporeale, S. Candel, Flame Describing Function analysis of spinning and standing modes in an annular combustor and comparison with experiments, Combust Flame 184 (2017) 136-152.
[25] A.H. Nayfeh, D.T. Mook, P. Holmes, Nonlinear oscillations, John Wiley & Sons, New Jersey, U.S., 1995.
[26] G. Ghirardo, M.R. Bothien, Quaternion structure of azimuthal instabilities, Physical Review Fluids 3 (2018) 113202.
[27] N. Noiray, M. Bothien, B. Schuermans, Investigation of azimuthal staging concepts in annular gas turbines, Combust Theor Model 15 (2011) 585-606.
[28] M. Bauerheim, M. Cazalens, T. Poinsot, A theoretical study of mean azimuthal flow and asymmetry effects on thermo-acoustic modes in annular combustors, P Combust Inst 35 (2015) 3219-3227.
[29] C. Paschereit, B. Schuermans, P. Monkewitz, Non-linear combustion instabilities in annular gas-turbine combustors, 44th AIAA aerospace sciences meeting and exhibit, 2006.
[30] T. Hummel, F. Berger, B. Schuermans, T. Sattelmayer, Theory and modeling of non-degenerate transversal thermoacoustic limit cycle oscillations, Thermoacoustic Instabilities in Gas Turbines and Rocket Engines: Industry Meets Academia, Munich, Germany, 2016.
[31] T. Hummel, F. Berger, M. Hertweck, B. Schuermans, T. Sattelmayer, High-Frequency Thermoacoustic Modulation Mechanisms in Swirl-Stabilized Gas Turbine Combustors—Part II: Modeling and Analysis, J Eng Gas Turb Power 139 (2017) 071502.
[32] G. Ghirardo, M. Juniper, J.P. Moeck, Weakly nonlinear analysis of thermoacoustic instabilities in annular combustors, J Fluid Mech, (2016) 52-87.
[33] N. Noiray, B. Schuermans, On the dynamic nature of azimuthal thermoacoustic modes in annular gas turbine combustion chambers, P Roy Soc A-Math Phy 469 (2013) 20120535.
[34] A. Faure-Beaulieu, T. Indlekofer, J.R. Dawson, N. Noiray, Experiments and low-order modelling of intermittent transitions between clockwise and anticlockwise spinning thermoacoustic modes in annular combustors, P Combust Inst 38 (2020) 5943-5951.
[35] G. Ghirardo, M.P. Juniper, Azimuthal instabilities in annular combustors: standing and spinning modes, P Roy Soc A-Math Phy 469 (2013) 20130232.
[36] M.R. Bothien, N. Noiray, B. Schuermans, Analysis of azimuthal thermo-acoustic modes in annular gas turbine combustion chambers, J Eng Gas Turb Power 137 (2015) 061505.
[37] G. Vignat, D. Durox, A. Renaud, S. Candel, High amplitude combustion instabilities in an annular combustor inducing pressure field deformation and flame blow off, J Eng Gas Turb Power 142 (2020) 011016.
[38] G. Ghirardo, H.T. Nygård, A. Cuquel, N.A. Worth, Symmetry breaking modelling for azimuthal combustion dynamics, P Combust Inst, (2020) 5953-5962.
[39] J.-w. Kim, W. Gillman, B. Emerson, D. Wu, T. John, V. Acharya, M. Isono, T. Saitoh, T. Lieuwen, Modal dynamics of high-frequency transverse combustion instabilities, P Combust Inst, (2020) 6155-6163.
[40] J. Kim, W. Gillman, T. John, S. Adhikari, D. Wu, B. Emerson, V. Acharya, M. Isono, T. Saitoh, T. Lieuwen, Experimental Investigation of Fuel Staging Effect on Modal Dynamics of

Thermoacoustic Azimuthal Instabilities in a Multi-Nozzle Can Combustor. Turbo Expo: Power for Land, Sea, and Air (2021), American Society of Mechanical Engineers.
[41] T. Indlekofer, A. Faure-Beaulieu, J.R. Dawson, N. Noiray, Dynamics of azimuthal thermoacoustic modes in imperfectly symmetric annular geometries, arXiv preprint arXiv:2104.07380, (2021).
[42] V. Acharya, M. Bothien, T. Lieuwen, Modal dynamics of thermoacoustic systems with closely-spaced eigenfrequencies, Thermoacoustic Instabilities in Gas Turbines and Rocket Engines: Industry meets Academia, Munich, Germany, 2016.
[43] T. John, G. Giulio, V. Acharya, M. Bothien, T. Lieuwen, Nonlinear dynamics of closely spaced thermoacoustic modes in the presence of noise, 11th U.S. National Combustion Meeting, 2019.
[44] A. Faure-Beaulieu, T. Indlekofer, J.R. Dawson, N. Noiray, Imperfect symmetry of real annular combustors: beating thermoacoustic modes and heteroclinic orbits, Journal of Fluid Mechanics 925 (2021).
[45] A. Faure-Beaulieu, N. Noiray, Symmetry breaking of azimuthal waves: Slow-flow dynamics on the Bloch sphere, Phys Rev Fluids 5 (2020) 023201.
[46] J.-F. Bourgouin, D. Durox, J.P. Moeck, T. Schuller, S. Candel, Self-sustained instabilities in an annular combustor coupled by azimuthal and longitudinal acoustic modes. Proceedings of the ASME Turbo Expo 2013, volume 1B: Combustion, Fuels and Emissions (2013), V01BT04A007-V001BT004A007, ASME GT2013-95010.
[47] J. Kim, W. Gillman, D. Wu, B. Emerson, V. Acharya, R. Mckinney, T. Lieuwen, M. Isono, T. Saitoh, Identification of High-Frequency Transverse Acoustic Modes in Multi-Nozzle Can Combustors. Turbo Expo: Power for Land, Sea, and Air (2020), American Society of Mechanical Engineers, V04BT04A051.
[48] N.M. Krylov, N.N. Bogoliubov, Introduction to non-linear mechanics, Princeton University Press, New Jersey, U.S., 1950.
[49] F. Culick, Nonlinear behavior of acoustic waves in combustion chambers—II, Acta Astronautica 3 (1976) 735-757.
[50] F. Culick, L. Paparizos, J. Sterling, V. Burnley, Combustion noise and combustion instabilities in propulsion systems, AGARD, Vol. 512, Neuilly sur Seine, France, 1992.
[51] F. Culick, V. Burnley, G. Swenson, Pulsed instabilities in solid-propellant rockets, J Propul Power 11 (1995) 657-665.
[52] T.C. Lieuwen, Experimental investigation of limit-cycle oscillations in an unstable gas turbine combustor, J Propul Power 18 (2002) 61-67.
[53] A. Peracchio, W. Proscia, Nonlinear heat-release/acoustic model for thermoacoustic instability in lean premixed combustors. Turbo Expo: Power for Land, Sea, and Air (1998), American Society of Mechanical Engineers, V003T006A022.
[54] A.P. Dowling, Nonlinear self-excited oscillations of a ducted flame, J Fluid Mech 346 (1997) 271-290.
[55] T.C. Lieuwen, Statistical characteristics of pressure oscillations in a premixed combustor, J Sound Vib 260 (2003) 3-17.
[56] A.H. Nayfeh, P.F. Pai, Linear and nonlinear structural mechanics, John Wiley & Sons, New Jersey, U.S., 2008.
[57] R.L. Stratonovich, Topics in the theory of random noise, CRC Press, Florida, U.S., 1967.
[58] P.D. Spanos, Stochastic analysis of oscillators with non-linear damping, Int J Nonlin Mech 13 (1978) 249-260.

[59] J. Roberts, P. Spanos, Stochastic averaging: an approximate method of solving random vibration problems, Int J Nonlin Mech 21 (1986) 111-134.
[60] J.G. Truxal, Automatic feedback control system synthesis, McGraw Hill, New York, U.S., 1955.
[61] V. Del Toro, S.R. Parker, Principles of control systems engineering, McGraw Hill, New York, U.S., 1960.
[62] J.E. Gibson, Nonlinear automatic control, McGraw Hill, New York, U.S., 1963.
[63] W.E. Vander Velde, Multiple-input describing functions and nonlinear system design, McGraw Hill, New York, U.S., 1968.
[64] P.E. Kloeden, E. Platen, Stochastic differential equations, Springer, New York, U.S., 1992.
[65] P. Clavin, J. Kim, F. Williams, Turbulence-induced noise effects on high-frequency combustion instabilities, Combust Sci Technol 96 (1994) 61-84.
[66] V. Burnley, F. Culick, Influence of random excitations on acoustic instabilities in combustion chambers, AIAA J 38 (2000) 1403-1410.
[67] T. Lieuwen, A. Banaszuk, Background noise effects on combustor stability, J Propul Power 21 (2005) 25-31.
[68] G. Bonciolini, A. Faure-Beaulieu, C. Bourquard, N. Noiray, Low order modelling of thermoacoustic instabilities and intermittency: Flame response delay and nonlinearity, Combust Flame 226 (2021) 396-411.
[69] G.E. Uhlenbeck, L.S. Ornstein, On the theory of the Brownian motion, Phys Rev 36 (1930) 823-841.